N.M.R. CHEMICAL SHIFT IMAGING

by

Bruce Robert Rosen

A.B., Harvard University (1977)

M.S., Massachusetts Institute of Technology (1980)

M.D., Hahnemann University (1982)

SUBMITTED IN PARTIAL FULFILLMENT
OF THE REQUIREMENTS FOR THE
DEGREE OF

DOCTOR OF PHILOSOPHY
IN MEDICAL ENGINEERING AND MEDICAL PHYSICS

at the

MASSACHUSETTS INSTITUTE OF TECHNOLOGY
June 1984

Signature of Author _____
Department of Medical Engineering and Medical Physics
April 26, 1984

Certified by _____
Alan C. Nelson
Thesis Supervisor

Accepted by _____
Ernest G. Cravalho
Chairman, Division Committee on Graduate Thesis

N.M.R. CHEMICAL SHIFT IMAGING

by

BRUCE ROBERT ROSEN

Submitted to the Department of Mechanical Engineering
in partial fulfillment of the requirements for the
Degree of Doctor of Philosophy in Medical Engineering
and Medical Physics

I. ABSTRACT

Methods of obtaining nuclear magnetic resonance (NMR) images containing chemical shift information are presented. Using a three-dimensional Fourier Transform approach (two spatial axes and one resonance frequency axis), proton chemical shift images were acquired in phantoms and in-vivo using both spin echo and free induction decay (FID) pulse sequences. A proton resonance frequency of 61.5 MHz, corresponding to a magnetic field strength of 1.44 tesla, was used. In simple phantoms, chemical shift images indicate that spectral resolution of 0.7 parts per million (ppm) is readily achieved at all locations within the image matrix, even when using a magnet not specifically designed for chemical shift spectroscopy. In-vivo images of normal human forearms and cat heads yield separable signals from water and lipid protons. In the cat brain, no appreciable NMR signal originates from membrane lipids (e.g., myelin); images acquired using FID pulse sequences imply T_2 relaxation times less than 2 msec for these protons. The measurement of magnetic susceptibility using this technique is also demonstrated. The effect of susceptibility variations in-vivo appears in general to be less than 1 ppm.

Proton chemical shift imaging was used to study fatty liver change in the rat. The correlation between lipid group signal intensity from chemical shift images in-vivo and liver triglyceride levels measured in-vitro was good ($r = .97$). In-vivo T_1 relaxation time measurements were made on lipid and water protons separately. Values calculated were corrected for the influence of gaussian plane selection and spin echo data acquisition, and demonstrate different T_1 times reflecting two distinct populations of non-exchanging protons. Proton chemical shift imaging offers enhanced sensitivity over conventional NMR imaging techniques in characterizing fatty liver disease.

Selective saturation (solvent suppression) techniques were used in an imaging context in both phantoms and in-vivo. Using a three-dimensional chemical shift imaging approach, data presented demonstrate the feasibility of imaging proton metabolites at low concentration. Phantom studies without solvent suppression failed to detect lactate at 80 mM; however with solvent suppression, lactate at 40 mM was imaged in a reasonable time (approximately 50 minutes). Using a conventional two-dimensional NMR imaging technique preceded by a selective (saturating) pulse, signal from water or lipid protons were eliminated (>95% reduction in signal intensity), resulting in images of $-CH_2-$ or H_2O proton distribution with resolution and imaging times equivalent to conventional proton images. With improvements in imaging systems, these techniques may play an important role in the non-invasive evaluation of tissue ischemia using proton NMR.

Table of Contents

II. Introduction

The Chemical Shift

Shortly after the demonstration of nuclear magnetic resonance by Purcell, Torrey and Pound, and Bloch, Hansen and Packard in 1946 (1,2), it was found that the resonance phenomenon was in a small but measurable way influenced by the chemical environment surrounding the nuclei being studied (3,4). The effect observed was the shift in the resonance frequency brought about from magnetic shielding of the nuclei by molecular electrons. More precisely, the frequency ω of the precessional motion of the nuclear magnetic moments can be predicted on the basis of their classical properties and is given by the Larmor equation:

$$\omega = \gamma B \qquad (1)$$

where γ is the gyromagnetic ratio (defined as the ratio of the nuclear magnetic moment to the spin angular momentum) and B is the magnetic field seen by the nucleus (5). This B field is traditionally rewritten so that equation 1 becomes:

$$\omega = \gamma B_o (1-\sigma) \qquad (2)$$

where B_o is now the strength of the applied magnetic field and σ is the shielding constant for the nuclei in a specific molecular environment, usually expressed in parts per million (ppm) relative to a standard reference. The value of σ lies in the range of 10^{-6} to 10^{-5} and is invariant with changes in B_o. Because this shielding varies depending on the exact electron configuration which in turn is influenced by the neighboring chemical groups, the amount of resonance frequency offset (the "chemical shift") can be correlated with the chemistry of the observed compound. Thus was born NMR spectroscopy, a tool of immense value to the analytical chemist.

In-Vivo NMR Spectroscopy

The importance of this tool was not lost on biochemists, molecular biologists and physiologists, and the biological implications of NMR spectroscopy were already understood more than 20 years ago (6,7). In the intervening years, NMR spectroscopy has been used *in-vitro* and *in-vivo* to study enzymatic reactions (8,9); measure intracellular pH (10,11); study cell membranes (12-14); follow metabolic pathways in normal, ischemic and neoplastic states (15-18); and monitor pharmaceutical interventions (19,20). Nuclei investigated include P-31, H-1, C-13, F-19, Na-23, and Cl-35. A recent bibliography of biological NMR references included about

6,000 titles (21), many of these reporting in-vivo determinations of NMR chemical shift spectra in specific pathologic conditions.

The technology allowing the acquisition of high spectral resolution NMR data for the study of biological systems in-vivo has evolved as the range of potential applications has grown. These techniques allow the acquisition of chemical shift data non-invasively from small localized volumes within intact biological samples. Three methods are commonly used today. In surface coil technology (18,19), a small receiving coil is used to acquire the resonance signal only from the tissue adjacent to the coil. TMR, or topical magnetic resonance, techniques use specially designed magnets to acquire chemical shift data from a volume lying deep within an animal (22). This technique uses time invariant higher order gradient field terms to define a small region of homogeneous B_o. Sensitive point techniques (23,24) are similar to TMR methods in that a small region of constant B_o is established, however unlike TMR this is accomplished by time varying linear gradient magnetic fields. P-31 has been most extensively studied using these three methods, with H-1 and C-13 receiving some attention as well.

NMR Imaging

Concurrent with these developments in in-vivo NMR

spectroscopy, the last 10 years have also seen the production of images using NMR. The first nuclear magnetic resonance images were produced by Lauterbur in 1973 (25) using a modified, conventional NMR spectrometer. The potential application of this technology to medical diagnosis was immediately apparent, since it had already been noted that NMR parameters [specifically, the proton (H-1) relaxation times T_1 and T_2] appeared to be altered in tumors when compared to corresponding normal tissues (26,27). In the ensuing years, advances in methods and instrumentation have resulted in the development of large scale NMR imaging devices which are now being used in clinical trials worldwide (28,29). To date, the vast majority of this work has investigated H-1, although recently Na-23 and P-31 images have been published (30,31).

Conventional NMR imaging systems modify NMR spectrometers by adding linear magnetic field gradients along each coordinate axis. With the use of these gradients, equation 1 can be rewritten to contain terms involving spatial position:

$$\omega(x,y,z) = \gamma(B_o + G_x x + G_y y + G_z z)(1 - \sigma) \qquad (3)$$

where B_o is the applied field strength in the absence of gradients, and $G_x = dB/dx$ is the slope of an applied linear gradient field along the x axis (y and z similarly). Thus in

the presence of linear gradients the precessional frequency will be a function of position; this frequency can be measured and used in spatially encoding NMR information to form an image (32). These gradients are relatively large (typically a few gauss over the usable magnet bore, thus gradient strengths vary according to magnet size from approximately .1-1 Gauss/cm), and they modify B_o to a much greater extent than σ, the chemical shift shielding. Because in conventional NMR imaging a gradient field along at least one spatial axis is present during the reading of the NMR signal, the chemical shift information is in general lost. However, not all information is significantly disrupted by application of field gradients.

Tissue Characterization

Unlike computed tomography, where signal intensity is related to the single parameter of X-ray attenuation, a number of variables influence the amount of signal seen from each given pixel on an NMR image (33). These include certain characteristics intrinsic to the tissue being imaged, such as the spin density, the longitudinal or spin-lattice relaxation time T_1 (a time characteristic of the return of the spin-system to thermal equilibrium), the transverse or spin-spin relaxation time T_2 (a time characteristic of the loss of phase coherence of the spin system), as well as flow

or motion within the sample. In addition, the exact nature of the sequential application of radiofrequency (RF) pulses (the pulse sequence) used to induce coherent nuclear precession interacts with these parameters to influence the observed signal. Since differences in signal between adjoining regions provides image contrast, and in particular allows for differentiation and specification of normal and pathological tissues, a significant effort has been undertaken to understand and categorize the intrinsic tissue parameters which influence the NMR signal.

Of these, the most important appears to be the tissue relaxation times T_1 and T_2. [A fine review of basic NMR relaxation theory can be found in Farrar and Becker (34).] With in-vivo imaging, relaxation times have been found to be significantly modified by malignancy (35-38), ischemic insult (37,39,40), and demyelinating disease of the nervous system (37,41,42). In many cases, the weighting of proton NMR image intensity with relaxation time variations appears to be a highly sensitive measure of tissue pathology. However, the specificity of relaxation weighted images, their ability to characterize the exact nature of the pathologic process present, is in question (43). To a certain extent this is due to lack of experience in image interpretation. Nevertheless, data seem to show a significant overlap in relaxation values obtained from diverse tissue disease

in-vivo (44).

From the above discussion, an apparent dichotomy of interest and specialization exists. On the one hand, NMR spectroscopic studies can be used to monitor and categorize function at the cellular level. On the other hand, NMR imaging offers superb anatomic detail and high sensitivity in detecting lesions. Furthermore, the very technique which allows for spatial encoding of the NMR signal to form an image disrupts the information essential to performing a useful spectroscopic study.

At first glance, this situation may not seem problematic. Spectroscopic and imaging studies, which contain different information, can be performed separately. A clinical protocol might involve first detecting a pathologic lesion with an imaging study, followed by spectroscopic analysis of the lesion in order to categorize it more fully if needed. This scenario suffers from two important limitations. First, the sensitive volume for *in-vivo* spectroscopic studies is imperfectly determined and localized. Surface coil technology has limitations on the depth of its sensitive region, and both TMR and oscillating gradient techniques are plagued by signal spillover and smearing in both spatial and frequency domains. Second, in at least some applications, an important consideration will be the size as well as character of an affected region. For example in ischemic insult, it

will be important to delineate the extent of both infarcted, non-viable regions and ischemic, viable areas for maximum clinical effectiveness. Even with adequate spatial localization such a spectroscopic analysis would entail a series of many measurements.

Chemical Shift Imaging

For these reasons it is desirable to develop techniques which allow for the acquisition of chemical shift information within an imaging context, which will be labeled chemical shift imaging. A simplistic approach to NMR chemical shift imaging would involve scanning a sensitive point step by step throughout the desired image plane or volume or, alternatively, would involve moving the object periodically through the sensitive region, thus obtaining an NMR spectrum at any number of points. This approach, however, suffers from the low sensitivity common to all point imaging methods (45). Furthermore, the techniques thus far proposed for electronic control of the location of the sensitive point (23,24,46) utilize radiofrequency (RF) pulse and field gradient control sequences which render the amplitudes of the spectral lines a complicated function of the relaxation times, making quantitative studies difficult (47).

Several techniques have been outlined in which the increased sensitivity of line, plane, or whole-volume imaging

is combined with chemical shift spectroscopy measurements (31,48-51). Such approaches allow NMR spectra to be extracted from all points within the image matrix or, alternatively, separate images corresponding to each of the chemically-shifted peaks may be displayed. However, one of these methods (49) is unsuitable for use with nuclei such as H-1 for which the chemical shift separations between constituent peaks are relatively small, or for which the natural linewidth in biological material is relatively broad. This is because the application of field gradients during signal acquisition, as proposed in this particular scheme, of necessity introduces additional line broadening and overlapping of peaks. Considerable mathematical analysis of the raw data is thus called for, and is of such a nature that system imperfections (especially noise and non-linear magnetic field gradients) can introduce severe artifacts. Other proposed techniques, such as those which utilize linear gradients in the radiofrequency field (50), depend upon a technology which still requires considerable development.

The Thesis in Preview

This thesis will present work accomplished at the Massachusetts General Hospital (MGH) to implement a practical method of chemical shift imaging. The nucleus of choice for these studies is H-1, for a number of reasons. Proton

imaging is the most widely performed and best understood NMR study in clinical use today. For this reason, comparisons between conventional NMR images and chemical shift images are more easily made, and the impact chemical shift images might have will be more readily assessed. In practical terms, the widespread dissemination of proton imaging technology will lead to a large number of NMR machines capable of performing proton chemical shift studies. Finally, although the typical chemical shift differences are much smaller for H-1 than for P-31 or C-13 (and hence more stringent requirements need to be imposed on the experimental parameters), H-1 has a much higher physiological concentration than these other nuclei (80 molar vs. ~ 20 mM for P-31) and has the highest NMR sensitivity of any stable nucleus.

This thesis will chart the development of proton chemical shift imaging techniques, from their mathematical basis through their application in studying various disease conditions. Chapter III will review the theory of chemical shift imaging, discuss the specific methods and techniques chosen to perform proton chemical shift imaging at the MGH, and present the hardware and software specifications of the imaging equipment used. Chapter IV will present the results of data acquired on phantom or test objects, and discuss the implications of various methodologic choices.

Chapter V will then display the first <u>in-vivo</u> proton

chemical shift images ever acquired, and the implications of these results to the study of diseased tissue will be analyzed. Chapter VI presents data acquired in the study of a particular pathologic condition, fatty liver change. Because relaxation time data for individual chemical species are calculated, an extensive Appendix addresses the problem of T_1 relaxation time determinations in plane selective NMR imaging. Chapter VII will discuss the application of a technique familiar to NMR spectroscopists, solvent suppression, in chemical shift imaging. This technique is used in phantom studies to image pathophysiologic concentrations of lactate, an important metabolic product under anoxic conditions, and to image fat and water distributions in-vivo with great efficiency. Finally, Chapter VIII reviews the data presented, and discusses the implications of this work for future clinical NMR studies.

III. Technique, Theory and Equipment

Technique of 3-Dimensional Chemical Shift Imaging

The technique used to acquire the chemical shift images reported in this thesis is a modification of the three-dimensional Fourier zeugmatography method outlined by Maudsley et al. (52) for the measurement of magnetic field distributions. Three dimensions of data are encoded and reconstructed; two spatial coordinates (for convenience labeled x and y) and a single frequency or chemical shift coordinate (labeled ω). For the imaging of three-dimensional objects, a planar selective excitation technique (53) is first used to remove redundancy of the third, non-encoded spatial coordinate.

There are three important modifications of the experiment as outlined by Maudsley. First, both x and y spatial coordinates are phase encoded, while the chemical shift coordinate is frequency encoded (54). This means that the NMR signal (spin echo or FID) is acquired in the absence of all applied gradients, with the result that the Fourier Transform of the time domain data reflects intrinsic chemical shift differences in resonant frequency. This is thus completely analogous to other pulsed or Fourier Transform NMR spectroscopic experiments (34). This modification was written out by Brown, et al. (51), to allow for chemical

shift imaging of phosphorus, and more recently by Maudsley et al. to perform field mapping (55). Second, the spin-warp method (56) of phase encoding is used, whereby the amplitude of the encoding gradient, and not its duration, is varied. The timing of events for each phase encoded pulse sequence is thus identical. Third, unless otherwise noted, experiments used spin echo data acquisition following application of a 180° refocusing broadband pulse. This does not affect the methods of dimensional encoding, however it does introduce a significant degree of T_2 weighting into the signal intensities measured (see Appendix).

A schematic of a generalized RF pulse sequence to perform this study is shown in Figure 1. The initial RF pulse in this sequence is a narrow bandwidth 90° pulse applied in the presence of a z axis magnetic field gradient in order to selectively excite an x-y plane. This pulse has a gaussian profile in time, and hence a gaussian distribution in its frequency spectrum. This has the disadvantage that spins on either side of the central plane are nutated by less than 90°. An important advantage is that all spins are approximately phase coherently independent of the tip angle (see Appendix). A second, 180° broadband RF pulse is applied some time later (½ TE, TE is equal to the time from initial excitation to the center of the signal echo) in order to facilitate transverse magnetization refocusing. The peak of

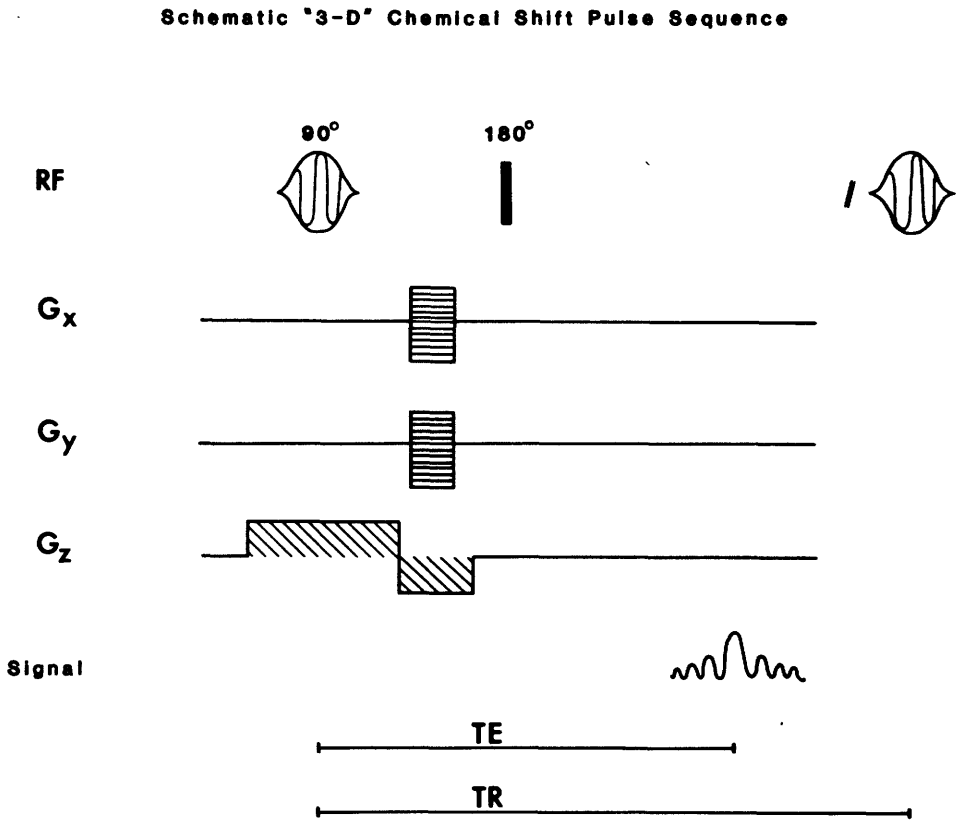

Figure 1. Schematic representation of generalized pulse sequence used to perform "3-D" chemical shift imaging. Note all gradients are off during data collection.

the resulting spin echo will then occur at equal time beyond this 180° pulse. Digital sampling can begin at the echo's peak, or sooner to allow centering of the signal echo within the data sampling period. The latter has the advantage of increased S/N, however, as will be discussed later, delaying data sampling offers some technical advantages.

The application of magnetic field gradients is also shown in Figure 1. An important observation is appropriate at this point. The exact locations of both the phase encoding gradient G_x and G_y, and the refocusing period of the plane selection gradient G_z, are not mandated. What is important is that to first order the first moment of G_z (the integral of G_z with time) be zero to allow refocusing of the spin echo (54), and that all gradients are off during data acquisition. Note also that a positive gradient applied before a 180° refocusing pulse is equivalent to a negative or oppositely sensed gradient applied after the 180° pulse. This allows for flexibility in gradient timings and strengths, an important consideration which will be discussed later.

Theory of Chemical Shift Imaging

The phase encoding gradients G_x and G_y described in the sequence above refer to a series of gradient pulses of equal duration but different amplitude. The function these stepped gradients have in encoding an image can be formulated as

follows. Because gradients must be off during signal acquisition to preserve chemical shift frequency differences, spatial position cannot be related to resonance frequency as is the case with conventional NMR imaging (57). Position can be encoded, however, by making the spin phase a function of position. For example, when compared to spins precessing within a uniform field B_o, spins found within a superimposed x axis gradient G_x will precess at a different rate, depending on their x axis coordinate and gradient strength. During this period these spins will accumulate a phase offset proportional to the difference in B and the length of time for which the spins experience a modified field. This is a simple reflection of the Larmor relation. More quantitatively, if these spins reside within G_x for a period τ, then the extra phase $\Delta\phi$ acquired due to this gradient is simply written from the Bloch equations:

$$\Delta\phi = \gamma G_x x \tau \qquad (4)$$

where x represents the spatial coordinate, and the term $G_x x$ is just the extra field superimposed upon B_o. γ is the gyromagnetic ratio.

By itself, a single spin phase cannot be used to uniquely describe spatial position. To understand how phase phenomena can be used to spatially encode NMR data, it is

necessary to explicitly write out the signal intensity measured during an NMR experiment on an x-y plane of precessing spins. For generality the possibility of different chemical shift frequencies δ is allowed. (δ is defined as = $\gamma B_o \sigma$, the frequency shift brought about by chemical shielding.) Transient gradients of the kind discussed above (labeled phase encoding gradients) may be applied along both x and y coordinates. Their amplitudes can be varied in this experiment by integer increments m and n (x and y axis). In a general sense one can write the signal intensity measured, a function of time t and the amplitude of the phase encoding gradients, in terms of the spatial distribution (x, y) of the object. By summing the intensity over the spatial extent of the object and paying attention to the spin phase, this signal is written:

$$S(t,m,n) = \iiint \rho(x,y,\delta) S_{xy\delta} \, dxdyd\delta \qquad (5)$$

where the phase term is:

$$S_{xy\delta} = \exp\{i(\delta t + k_m X + k_n Y)\}$$

and where $\rho(x,y,\delta)$ is the density distribution of the object in the 3 space which includes the chemical shift frequency dimension δ . It can also be thought to

include appropriate relaxation influences on signal amplitude. The term δt is the phase contribution with time from spins at resonance frequency δ . Also defined are:

$$K_m = \gamma\ m\ G_x\ \tau$$
$$K_n = \gamma\ n\ G_y\ \tau$$

The terms $K_m x$ and $K_m y$ are by equation 5 the amount of extra phase contributed to the spin system at coordinates (x, y) by the mth or nth phase encoding gradient step. τ here again is the gradient duration, G_x and G_y the unit gradient amplitude of each step, and γ the gyromagnetic ratio of the nucleus being imaged. Oscillation at the resonance frequency $\omega = \gamma B_o$ will modulate S(t,m,n).

A closer look at equation 2 reveals that S(t,m,n) is just a single point in the three-dimensional Fourier Transform of the object described by $\rho(x,y,\delta)$. By sampling this function at sufficiently inclusive values of t, m and n, a discrete "image" of this frequency space object can be acquired. By the transform theorem, if we then take the Fourier Transform of this discretely sampled object we will acquire a representation of the original object ρ in x, y and δ . The presentation of the chemical shift frequencies δ is most important, and is a direct result of sampling in the absence of applied gradients.

The representation of $\rho(x,y,\delta)$ will of course be subject to the errors inherent in discrete sampling of S(t,m,n) such as aliasing, and resolution will be limited by the finite sampling of t, m and n. These parameters can be set (within finite limits) for each experiment. Just what values for sampling are appropriate will be addressed later. Data reconstruction consists of Fourier Transforming the NMR signal versus time into signal intensity versus frequency, then transforming the two addition coordinates (so-called pseudo time axis) of data, encompassed by the switching of G_x and G_y through a rectangular array of values for each frequency sampled. (These transformations can actually be performed in any order).

Data Representation of 3-Dimensional Image Matrix

The results of the three-dimensional Fourier Transformation of the raw data is an image matrix of the form shown in Figure 2. Image data corresponding to a particular spectral peak (a "δ-image") are distributed about a curved surface; the precise shape of the surface is defined by the static field non-uniformities within the selected slice. The width of the distribution of data either side of this surface will depend on the linewidth of the particular peak. As in conventional NMR spectroscopy, both intrinsic (sample-related) line-broadening mechanisms and static

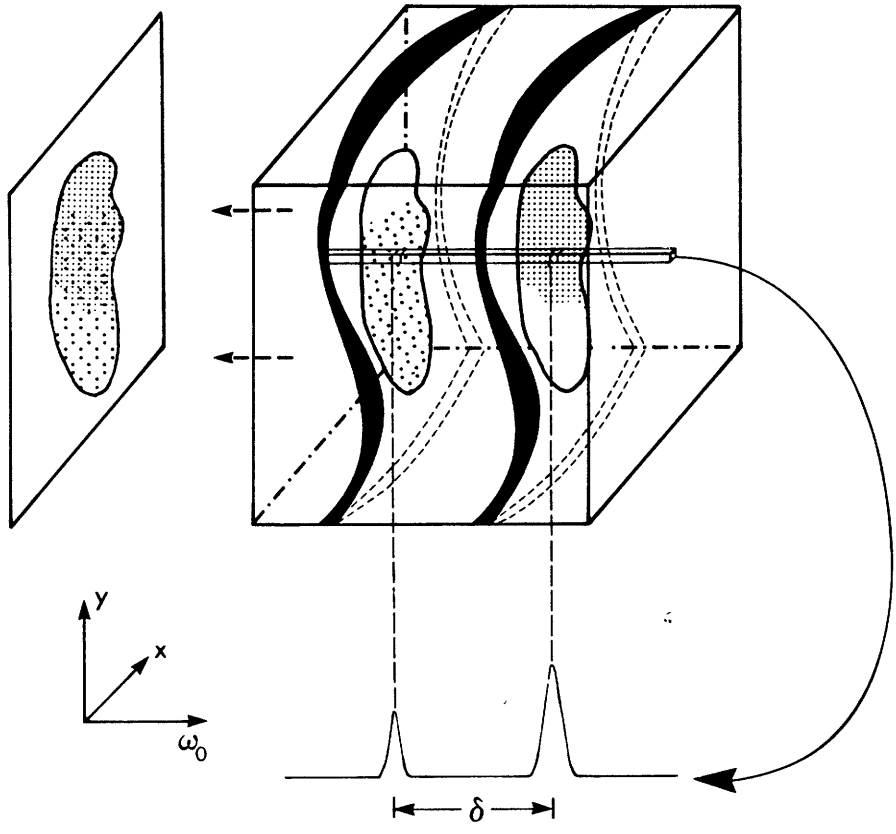

Figure 2. (a) Three-dimensional image matrix formed by Fourier transformation of the raw data. Two spatial axis (x,y) and the frequency axis (ω) are displayed. An object with two chemical shift spectral peaks is represented. In (b), information is summed along ω to form a conventional, non-chemical shift image. Spectral (ω) information can be extracted from any (x,y) point - this is shown in (c).

magnetic field heterogeneities (ΔB_o) define this width. Note, however, that in this case the line-broadening contribution from ΔB_o depends only on the magnetic field non-uniformity over any given pixel which, since the pixels may be made almost arbitrarily small, will usually be very much less than the non-uniformity in B_o extant over the whole imaging volume. The effect of this latter heterogeneity is to shift the NMR spectra arising from each of the pixels relative to one another. Indeed, this provides the basis for mapping the magnetic field distribution discussed by Maudsley et al. (55). When more than one resolved peak exists in the NMR spectrum, the separate δ-images will each be distributed about similar curved surfaces, parallel to one another and separated by their chemical shift differences.

The more usual NMR image may be derived by integrating the NMR spectrum at each pixel location. This corresponds to the projection of all the various δ-images onto a plane orthogonal to the chemical shift axis, and may be obtained simply by summing all of the reconstructed image data planes. Data contained in ω-x and ω-y planes are labeled "edge profiles," and these reveal the extent of field non-uniformity as well as chemical shift information along a single line in the (x,y) plane.

The above discussion describes in general terms the method and results of "3-D" chemical shift imaging. The

details of each experiment are discussed in appropriate sections to follow.

Equipment: Hardware

The NMR imaging equipment used throughout this thesis was assembled by the Technicare Corporation, Solon, Ohio, and located at the Massachusetts General Hospital, Boston, Massachusetts. The basic components of an NMR imaging system are reviewed by Pykett (58) and include the main magnetic and gradient field subsystems, radiofrequency source and RF coil, and computing and interface subsystems. The important properties of each component, relevant to this thesis, are discussed below.

The magnet used for all chemical shift studies was a horizontal bore, 1.44 tesla superconducting magnet built by Oxford Instruments. This prototype animal system has a usable 8 cm bore after inclusion of gradient and RF coils. Shimming was performed with the use of 8 superconducting shims; no room temperature shims were available. The homogeneity over a small (~ 1 ml) central volume is <Ø.5 ppm. Over a 7 cm image plane of thickness <Ø.5 cm, this value is increased to almost 5 ppm.

Gradient fields are under computer control, with maximum amplitude of 1 gauss/cm, changing at a maximum rate of Ø.5 tesla/sec for each axis. The RF coil is of self-resonant

design, and tuned to the appropriate proton resonance frequency of 61.5 MHz. The controlling CPU for the NMR imager is a PDP 11/34, configured for these studies with a single 160 M byte fixed disk, 10 M byte removable disk, and Floating Point Systems Array Processor to permit high speed image reconstruction.

Equipment: Software

Software and hardware interfaces between the CPU and imager were designed, written and built by the Technicare Corporation. Although the details of these systems are beyond the scope of this thesis, certain aspects of the software control in particular are important. Foremost among these is the pulse, gradient, and data acquisition software. In general terms these programs allow for control of the RF pulses and gradient fields applied, and certain data acquisition parameters. RF pulse control is separated into two categories, hard (broadband) pulses, and soft (shaped or profiled) pulses. Both can be independently set as to pulse duration (hardware limited currently to 8 msec), frequency (in 1 Hz units), RF phase (in multiples of 90^{o}), and degree of transmitter power attenuation. Profiled pulses can additionally be tailored as to their amplitude versus time function; a gaussian distribution is routinely used unless otherwise noted. Gradient field strengths can be programmed

independently along all three spatial axes (x, y, z). In addition, gradient programming for successive intervaled amplitudes, as used in spin warp imaging (see Theory) is user-determined. The range of such steps is 2^n (n = 3 - 8), allowing for FFT reconstruction of phase encoded coordinates.

Data acquisition parameters under user control include the sampling interval (time between A-D sampling of the NMR output signal, range <240 msec), the total number of samples collected for each projection of the image data set [range 2^n ($n \leq 10$)], the number of signal averages per projection, and the total number of image data sets acquired during each experiment. Projection is used here to refer to data acquired for a single value of (phase encoding gradients) m and n. Hardware limits the total number of samples per projection for all data sets to 1024, leading, for example, to a limit of four images per single experiment if 256 points are sampled/projection for each image. Additional control includes the amount of receiver attenuation applied before A-D conversion (ADC is nominally 12 bits), and timing delays to control the exact start of the data acquisition period.

The basic timing unit for all events within a pulse sequence (the generic term for the RF, gradient and data acquisition intervals) is the sampling interval (SI). This time determines an integer multiple period for all events. Excluded are the RF pulse lengths, which have independent

control in 1 μs units, but which cannot be repeated faster than the SI. In addition, CPU and interface timings limit the minimum event interval to >500 μs.

Within these broad confines a considerable degree of flexibility exists in the design of pulse sequences used for imaging. Although less flexible, data reconstruction and display software are capable of performing two- and three-dimensional Fourier reconstructions and displaying arbitrary two-dimensional planes through reconstructed 3-dimensional data on a high resolution video monitor. Archiving is via disk or 9-track tape, or film. Zero and first order phase corrections can be applied to the frequency domain data prior to reconstruction [multiplication of the complex (absorptive and dispersive) frequency transform by $e^{i\theta}$ and $e^{i\omega\theta}$ respectively]. Software also exists to manipulate two-dimensional displayed images, including region of interest (averaged signal intensity over a user-defined area) and image summation programs. Certain limitations in the ability to manipulate raw and reconstructed data do exist; these are discussed in more detail in appropriate later sections.

IV Phantom Data

Phantom Data: Background

To test the correspondence between imaging theory and practical considerations when using the 1.4 T imager at the MGH, model objects or phantoms were employed prior to *in-vivo* imaging tests. Data acquired from phantoms were used for a variety of purposes. First, the work of establishing the basic feasibility of proton chemical shift imaging on existing equipment was demonstrated on inanimate objects of infinite patience. Second, efforts to improve upon or expand the range of chemical shift imaging studies, including different data acquisition schemes, were facilitated by the use of stable objects. This allowed for easy comparison of new data with previous results. Third, basic NMR phenomena and machine response parameters were tested under the well-controlled and documented conditions that phantom objects could provide. From this, potentially subtle *in-vivo* effects could be studied under more rigorous circumstances, as a prelude to future studies with more sophisticated equipment.

Over an extended period, hundreds of proton chemical shift imaging experiments were performed on phantom models. This chapter will focus on those of greatest importance according to the above criteria.

Ethanol Phantom

The two-carbon alcohol, ethanol (CH_3 - CH_2OH), provided a simple but effective model to test the basic feasibility of performing chemical shift imaging studies on the MGH imager. Ethanol was chosen for a number of reasons. Historically, ethanol was one of the first compounds to be studied with the "high resolution" NMR spectrometers of 30 years ago, allowing one of the earliest determinations of the resonance frequency shift imparted by differences in electron shielding of the proton nuclei. Practically, ethanol is characterized by a long T_2 and reasonable T_1 (~ 2 sec) favorable for imaging. The three chemical shift peaks corresponding to the three proton types (CH_3, CH_2, and OH) are well separated but by differing amounts, providing the opportunity for quantitative correlation with measured results. Finally, it is inexpensive, readily available, and (relatively!) non-toxic.

The first few months of chemical shift imaging at the MGH saw a significant evolution in the pulse sequences used for these studies. The pulse sequence used with greatest success in these preliminary studies, and in subsequent in-vivo studies as well, is shown in Figure 3, and is labeled DELS.

Pulse Sequence and Image Parameters: Spin Echo Acquisition

Sequence DELS was based, as discussed in Chapter III, on

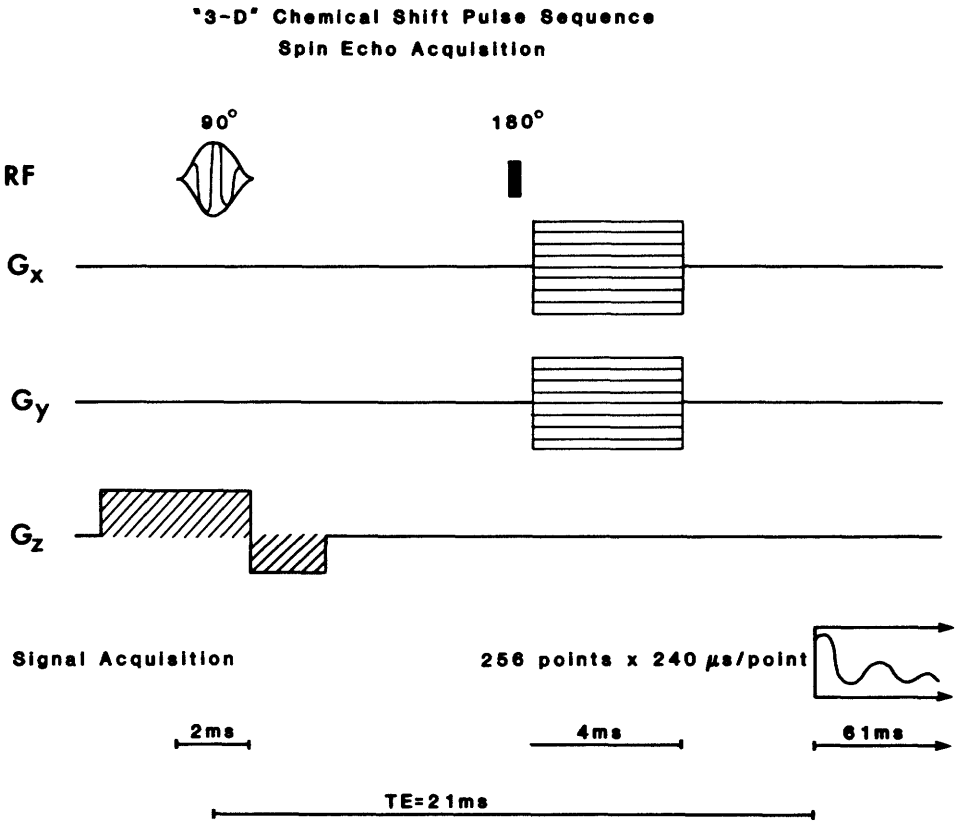

Figure 3. DELS, pulse sequence using 180° pulse refocusing. TE = 21 msec, while TR could be varied. Phase encoding gradients are on after the 180° refocusing pulse. Data collection begins at the spin-echo peak, and continues for 61 msec.

the 3-D FT approach to chemical shift imaging. Of importance, spin echo data acquisition was used in this sequence, with a TE time (90^{o} - echo peak interval) of 21 msec. This was kept short to minimize spectral intensity changes due to spin-spin or J coupling (34) between the proton peaks (which modulates the amplitude of spin echo signal intensities at a rate equal to the homonuclear coupling constant, about 5 Hz for ethanol), and to increase S/N by minimizing T_2 relaxation. The sampling interval and number of samples acquired per echo were determined by the requirements for spatial resolution and frequency bandwidth. Because proton resonance frequencies of most compounds lie within a 10 ppm range, and B_o inhomogeneity was measured to be no greater than this, the total bandwidth could in principle be kept quite small, < 20 ppm (1200 Hz at 60 MHz). This implied that the sample interval must be less than 417 μs. The use of the machine limit of a 240 μs sample interval implies that the signal is somewhat over-sampled. Since spectral resolution of < 0.5 ppm (30 Hz) could be hoped for from homogeneity measurements over small volumes, a total sampling period of 61 msec (256 samples) was chosen, leading to 16 Hz/data point.

However, with a sampling interval of 240 μ sec and 256 sampled points/echo, the total sampling period of 61.4 msec could not be centered about the echo peak. In addition,

transverse magnetization components which appear after the 180° pulse due to RF inhomogeneity make it undesirable to begin data sampling immediately following this pulse. For these reasons data collection was begun at the echo peak.

There are two important consequences of data uncentered with respect to the time domain. First, by sampling beginning with the echo peak amplitude, dispersive (imaginary) components in the Fourier Transform frequency spectrum are non-zero. These components are significantly broader in frequency than the absorptive (real) line spectrum. For this reason reconstruction should preferentially be carried out with the absorptive or real data being displayed to avoid the spectral line broadening that would result from display of the absolute magnitude of the frequency spectrum. Second, the above dictates that all spectral lines be in phase with one another to avoid phase determined intensity variation possible with real data display. This is accomplished by beginning data acquisition at exactly the echo peak. In practice, this was determined empirically by adjusting the start of the data acquisition period until the phase of all spectral peaks was equalized.

The z axis gradient strength during plane selection was set in pulse sequence DELS to excite a 1.5 mm (FWHM) thick plane with a gaussian selective pulse duration of 2000 μs. Phase encoding (x and y) gradients were placed after the 180°

refocusing pulse to smear or dephase any residual transverse magnetization which results from RF inhomogeneity of this pulse. In retrospect this may be more easily accomplished by refocusing along the z axis at this time. The amplitude of these gradients was adjusted to scale images identically to that found in conventional 2-D images.

Using sequence DELS, an Erlenmeyer flask of absolute ethanol was imaged. Because of the long (~ 2 sec) T_1 relaxation time of this pure liquid, the 90^{o}-90^{o} pulse interval, TR, was set to 2.6 seconds, to reduce T_1 relaxation effects on line signal intensity. Sixty-four phase encoding steps in x and y were acquired, resulting in a 64x64 square image array in the x-y plane. Imaging time was 183 minutes.

Results

An edge profile (ω -y plane) through the center of this circular cross-sectioned phantom is displayed in Figure 4. A number of important observations can be made from this image. First, the measured distance between the three spatial peaks on this data set is:

		Measured	Actual	Error
$(CH_3 - CH_2)$ppm	=	2.4	2.5	-Ø.1
$(CH_2 - OH)$ppm	=	1.8	1.5	Ø.3

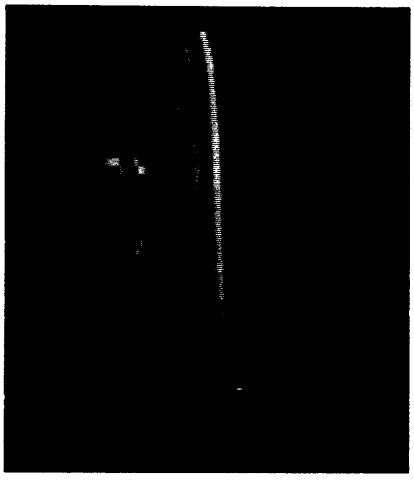

Figure 4. Edge profile (ω ,y plane) data through the center of an ethanol phantom acquired using DELS. The three lines correspond to the three chemical species (CH_3, CH_2, OH) of protons contained in ethanol. Curvature of the lines reflects B_o heterogeneity from pixel to pixel, while line widths reflect B_o inhomogeneity within each pixel.

These data are in good agreement with actual values and errors are within those expected on the basis of B_o homogeneity measurements. Second, the signal intensity values for the three peaks are not the expected 3:2:1, and is in fact closer to 2:1:1. This difference is in large part due to differences in spectral peak relaxation times, since both spin echo data acquisition and a partial saturation pulse interval (< 5 T_1) lead to T_2 and T_1 effects (respectively) on line height. Increasing TR to 4.5 seconds leads to nearly a 3:2:1 ratio (see multiphantom results), indicating T_1 effects dominate. The most important observation is that the basic technique works, and that despite overall poor homogeneity in the magnet (shown by the curvature in the edge profile), spectral resolution on the order of 1 ppm was possible, with relative chemical shift differences measured to within 0.3 ppm.

Pulse Sequence and Image Parameters: FID Acquisition

In order to be able to measure spectral lines of very short T_2 (< 5 msec), Hahn spin echo techniques were supplanted with a pulse sequence designed to measure a free induction decay (FID) following a single 90° pulse. Although this capability was developed to address certain *in-vivo* questions discussed later, the pulse sequences utilizing a gradient refocused acquisition method were tested first using

the familiar ethanol phantom.

The pulse sequence used for FID acquisition, labeled DELVS, is shown in Figure 5. In this sequence the phase encoding x and y gradients, and the z refocusing gradient, are concurrent. The total time elapsing between the exciting pulse and the start of data acquisition (labeled TE in these FID experiments) is only ~ 5 msec. In this sequence, data acquisition begins at the point of maximum signal. This occurs (in the absence of phase encoding gradients) when the z refocusing gradient exactly compensates for the dephasing of spins along the z axis which occurs during slice selection. As this gradient is applied and rephasing occurs, a reappearance of the NMR signal appears. Here, however, the resulting signal echo is gradient, and not 180^{o} pulse, refocused. The importance of this is discussed below.

As before, 256 data points were collected, with a sampling interval of 240 μ s. In order to speed up data collection and more nearly resemble <u>in-vivo</u> conditions, a small quantity of $CuSO_4$ was added to the ethanol to decrease the net T_1 relaxation time to 500 msec. TR was set to 300 msec, and with 64x64 phase encoded steps imaging time was 21 minutes. At this TR, T_1 effects on spectral line intensity become significant, and so no conclusions can be drawn about relative proton density. T_2 effects are quite small however (TE = 5 msec).

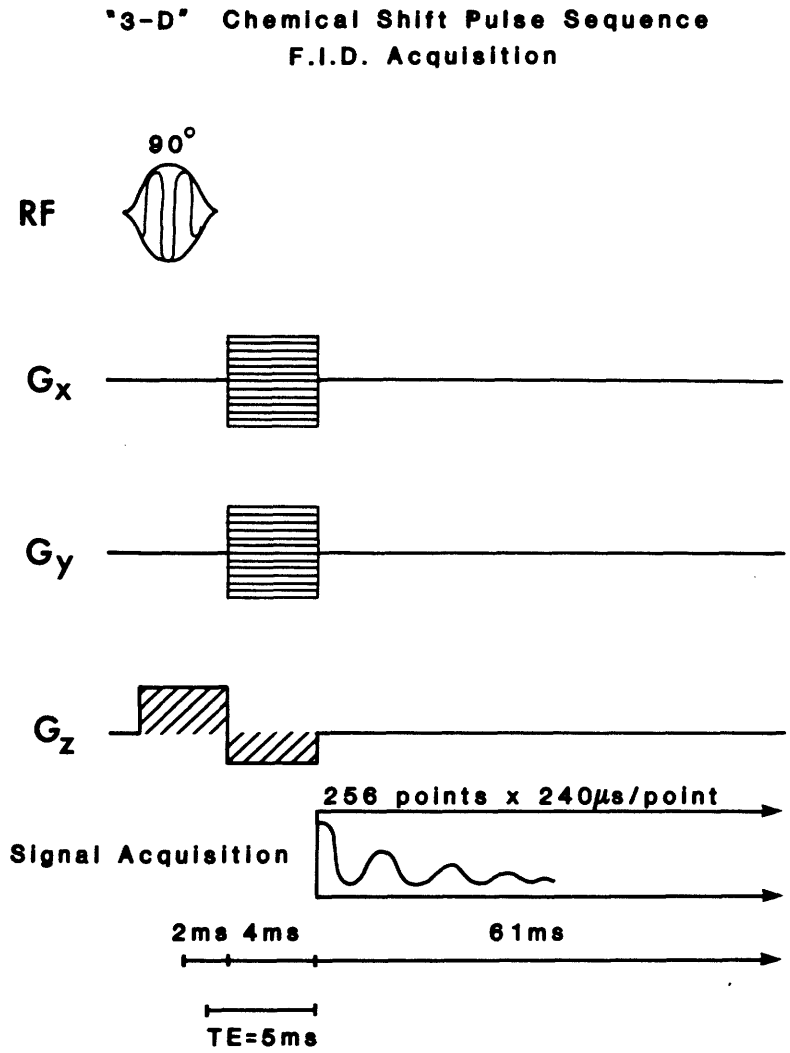

Figure 5. DELVS, pulse sequence using gradient refocusing ("FID" acquisition). TE = 5 msec, with variable TR. Phase encoding and z axis refocusing occur concurrently. Data collection begins at the signal peak, and continues for 61 msec.

Results: FID Acquisition

The results of the above experiment are shown in Figure 6. The first observation is that, as before, the three lines of the ethanol chemical shift spectrum are present. However, compared to the previous image (Figure 4) spectral resolution is significantly worse. Two effects are present.

As in the previous sequence, data acquisition begins at the signal peak, and hence line broadening is present when displaying the absolute magnitude of the reconstructed image (6c). Unlike the previous sequence, in sequence DELVS a significant phase artifact appears across a single x-y image plane (6b), and an edge profile ω -y image (6a) when the real data are displayed. There are two different phase shifts observed. The more important of these is the phase difference in moving about the x-y plane. This is seen as the striping on Figure 6b. The cause of this phase incoherence across the image plane is clear, when the difference between the "FID" (gradient echo) (DELVS) and 180° pulse (Hahn) spin echo (DELS) experiments is considered. In both, a signal echo is formed sometime after the initial 90° pulse. However in DELVS, this is performed by gradient reversal only. The difference between an echo formed by this process and one formed following a 180° pulse is that the

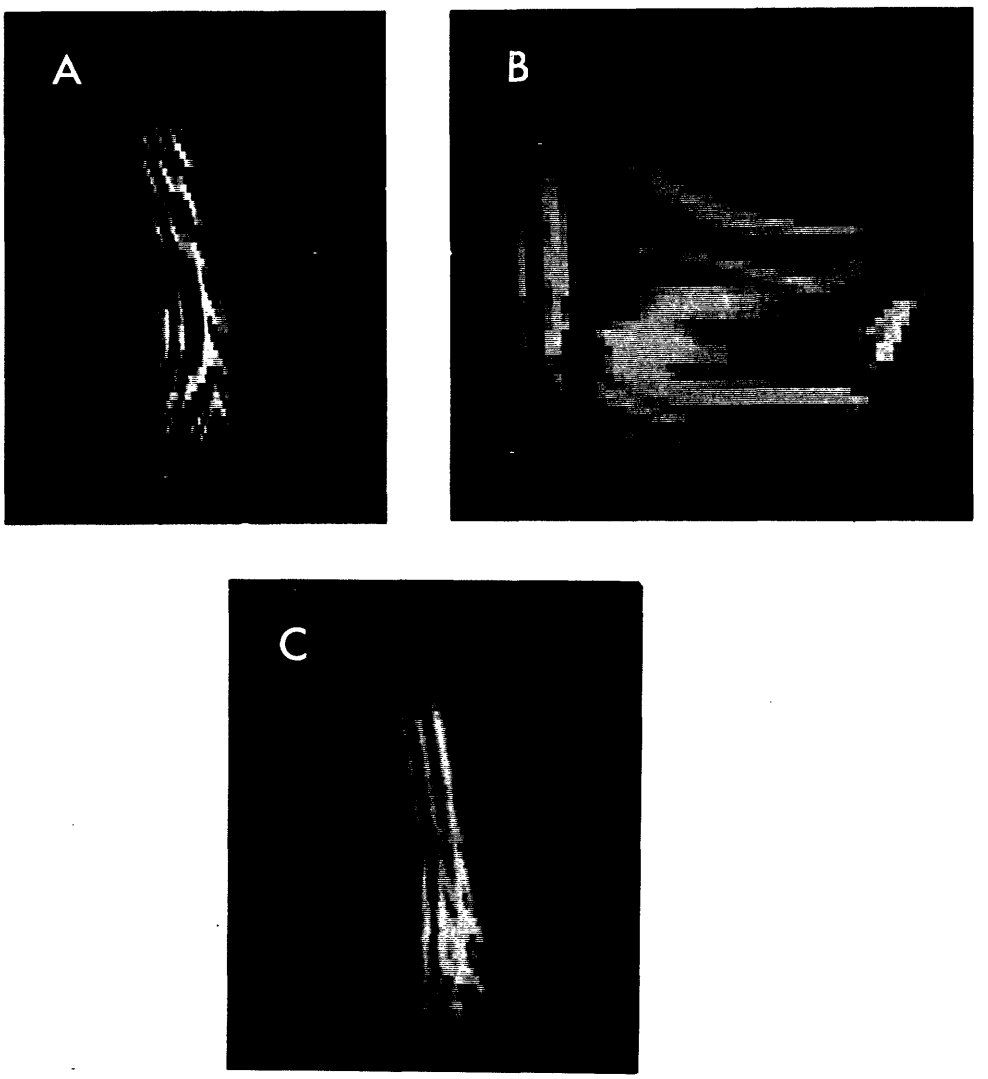

Figure 6. Three views of an ethanol phantom acquired using DELVS. On top are displayed (a) edge profile (ω -y) and (b) δ -image (x-y) plane through the phantom. The real (absorptive) data only is displayed here. Alternating light and dark bands reflect changes in phase across these image planes. In (c), edge profile (a) is redisplayed, this time with the absolute magnitude of the data shown. Line widths are somewhat broader, but phase artifacts disappear.

latter corrects for all static inhomogeneities in B_o (34). The process of gradient refocusing corrects only for the spin dephasing caused by the applied gradients, and not for inhomogeneities present in the absence of gradients.

There are two consequences of gradient refocusing. First, the amplitude of a spin echo formed by gradient reversal only will decrease with time constant T_2^*, a time shorter than the actual sample T_2 by the degree of B_o inhomogeneity. For this reason signal amplitude will be slightly decreased when compared to a Hahn spin echo experiment with the same TE. More important for understanding the above experiment, any phase shifts accumulated due to spatial B_o variations are not corrected for in DELVS, and thus the phase of the resulting echo will be position (B_o) dependent. This is exactly what is seen in Figure 6b. The phenomenon of position dependent phase on gradient refocused "FID" signals was also experimentally verified on small samples moved across the field using the same pulse sequence without phase encoding gradients. The magnitude of the effect can be calculated as follows. If a 180^o phase shift is postulated (white to black on image data), what ΔB_o is needed over the TE of DELVS? Assuming a resonance frequency of 60 MHz, and TE = 5 msec, then by equation 4 (Chapter III):

$$\Delta B = \Delta\phi/\gamma\ TE$$

or in ppm:

$$\Delta\ ppm = \Delta\phi/\gamma\ TE\ B_o \times 10^{-6} \qquad (6)$$

For the above conditions, Δ ppm = 1.6 ppm. Thus at high resonance frequencies (large B_o) only small inhomogeneities are needed to induce large phase shifts, even over short periods of time. Certainly inhomogeneities of this order exist across the x-y plane, and hence phase offsets of the kind seen in Figure 6b are expected. In fact, this kind of phase mapping can be a much more sensitive way of plotting B_o heterogeneity than the resonance frequency offset along the ω axis proposed by Maudsley, especially if TE is large. The concept suffers from 2 π ambiguity; however, this could be eliminated by repeated scans with different TE. This would then be the analogue of optical methods of uniformity measurement. This process could also be carried out using conventional (x-axis frequency encoded) imaging methods. However, because gradients cannot be switched on instantaneously (rise times are typically 1 msec), G_x would need to be on slightly before the signal is read, to assure that frequency encoding occurs during a period of uniform gradient. For this reason, a small amount of phase encoding

will occur along x, which while of first order and hence correctable, cannot practically be separated from a linear inhomogeneity in B_o along the x direction without a detailed knowledge of G_x with time. To my knowledge, the idea of phase detection homogeneity mapping has not been proposed previously.

The second phase offset, seen well in Figure 6c, is a phase shift between each spectral peak. This leads to a "barber pole" appearance, a diagonal tilt to the phase defects induced along the spatial (here y) axis. This ω axis phase offset is due to the different resonance frequencies reflected by position along ω. The magnitude of this phase effect can be estimated from a simple example as follows. In describing plane selection via a gaussian RF envelope, it was noted that the time needed to gradient refocus the signal was one-half the time the RF was on, assuming a refocusing gradient of equal magnitude but opposite direction (55). During the period of RF excitation, regions with different chemical shifts will precess on average at the same frequency (the central RF frequency). However, a slightly different x-y plane will be excited for each resonance peak, the z-axis separation depending upon the magnitude of G_z on during the RF pulse [G_z(RF)]. Dephasing of spins along ω begins when the RF is turned off and G_z is reversed [G_z(re)]. This dephasing is again described by equation 6, but with an

important difference. The Δ ppm term in equation 6 is now 2x the intrinsic chemical shift difference, since an additional factor of Δ ppm is added by the effect of G_z on spins with different z coordinates. This effect is of course exactly equal to Δ ppm (chemical shift), since this intrinsic frequency difference led to the chemical shift offset along z, and $G_z(re) = G_z(RF)$ in this example. Rewriting equation 6 with this included leads to:

$$\begin{aligned} \Delta\phi &= (2\Delta \text{ ppm})\, \gamma\, B_o \times 10^{-6} \times t(re) \\ &= \Delta \text{ ppm}\ \gamma\, B_o \times 10^{-6} \times t(RF) \end{aligned}$$

where t(re) is the refocusing period = $\frac{1}{2}$ t(RF), t(RF) being the duration of the plane selective RF pulse. In the more general case where $G_z(re) \neq G_z(RF)$, and hence $t(re) \neq \frac{1}{2}t(RF)$, the phase term due to the presence of $G_z(re)$ is constant, since the product $G_z(re) \times t(re)$ must be constant for refocusing to be complete. However, the intrinsic chemical shift differences will lead to dephasing proportional to the time between excitation and signal acquisition, hence equation 7 can be rewritten:

$$\Delta\phi = [\tfrac{1}{2}\, t(RF) + t(re)]\ \Delta \text{ ppm}\ \gamma\, B_o \times 10^{-6} \qquad (8)$$

For a chemical shift difference of 3.5 ppm, two peaks will be

offset in phase by 375^{o} given the t(RF) and t(re) timings of DELVS. This is consistent with the results of Figure 6a.

By displaying the magnitude of the image data after reconstruction, both of the phase artifacts discussed above can be eliminated, although as already discussed the presence of non-zero dispersive elements in the spectra will result in broadening of the spectral lines. While not ideal, Figure 6c does demonstrate that the broadening using DELVS is not critical for peaks separated by more than about 2 ppm.

Multiphantom: Design, Pulse Sequence, Image Parameters

In order to test the ability of chemical shift techniques to resolve differences in spectral content across a single image, a phantom consisting of four test tubes that contained methanol (CH_3-OH), ethanol (CH_3-CH_2-OH), n-butanol (CH_3-CH_2-CH_2-CH_2-OH) and water (25% by volume of distilled H_2O in D_2O) was constructed. The inside diameter of each tube was 15 mm, and all tubes were surrounded by D_2O. Because of its better frequency resolution, images were acquired using DELS. The relatively long T_1 of the pure samples dictated a long pulse interval, and so TR was set to 5.Ø seconds. 64 x 64 gradient pulse encoding steps were used, with the total imaging time equal to 5.9 hours.

Results

An acquisition obtained using the above imaging parameters yielded the data shown in Figure 7. An integrated (x-y) image is shown, with selected edge profiles displayed alongside; they show data contained within parallel, ω -y planes. The edge profile displayed to the left of the integrated image has an x-axis coordinate which passes through the tubes containing n-butanol and methanol. The edge profile on the right has an x-axis coordinate which passes through the tubes containing water and ethanol. Static B_o heterogeneity is again responsible for curvature of the edge profiles, however the heterogeneity over a given voxel (~ 2.5 mm^3) is sufficiently small to enable spectral resolution of the major proton resonances. Figure 8 shows the chemical shift spectra extracted from a small region of interest (ROI) in the center of each tube; note that the areas under the peaks are again slightly modified by relaxation time effects.

The above data were collected using a slice thickness (z axis) of 1.5 mm. When the section thickness was reduced to Ø.8 mm (yielding a volume element of 1.3 mm^3), the high field n-butanol signal was split into the expected two resonance peaks with separation of Ø.7 ppm (bottom spectrum, Figure 8). This spectrum compared favorably to one obtained with n-butanol on a 6Ø MHz dedicated CW NMR spectrometer. Sweep time was 25Ø seconds (see Figure 9). The width of the

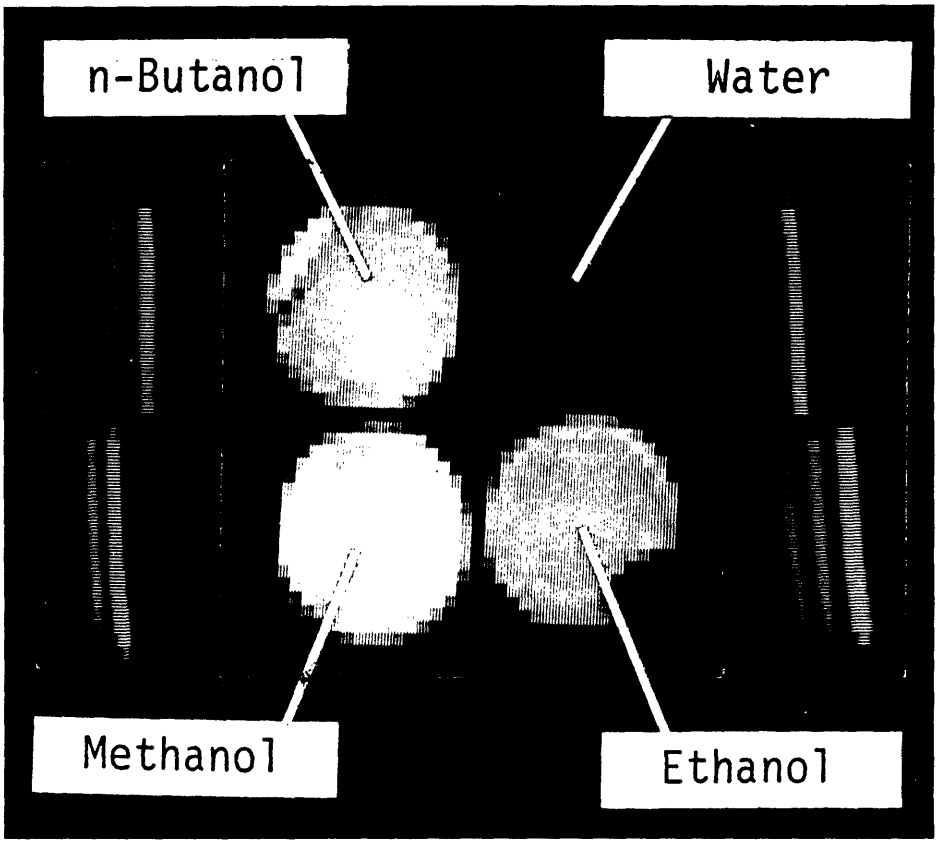

Figure 7. Results from the multiphantom experiment. Centrally, an integrated (x-y) is shown, with selected edge profiles through each tube alongside. Chemical shift resolution of the major proton peaks is easily seen.

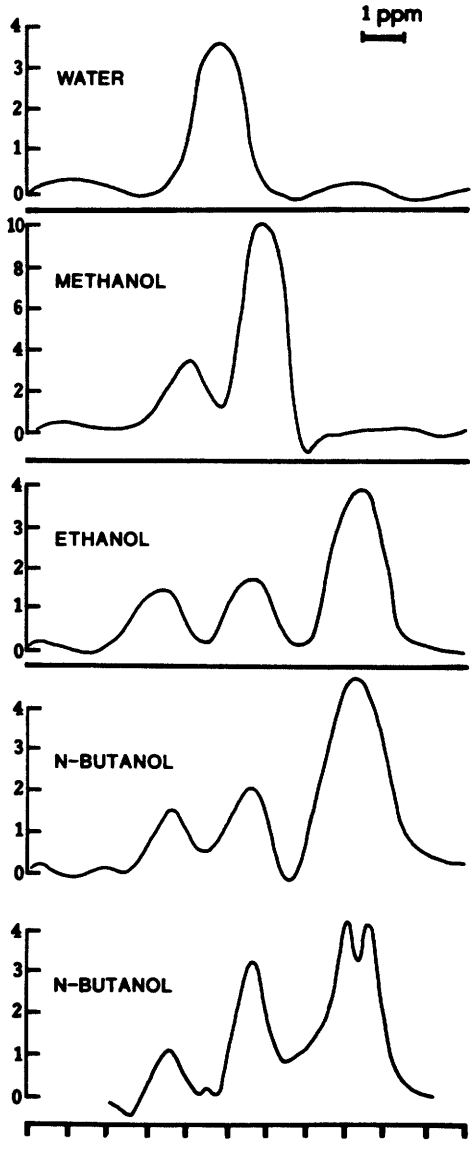

Figure 8. Chemical shift spectra extracted from 2 x 2 pixel (x,y) regions within each of the four compounds tested. The thickness used to acquire the first four spectra shown was 1.5 mm. When reduced to Ø.8 mm, the high field peak of butanol was just resolved (bottom).

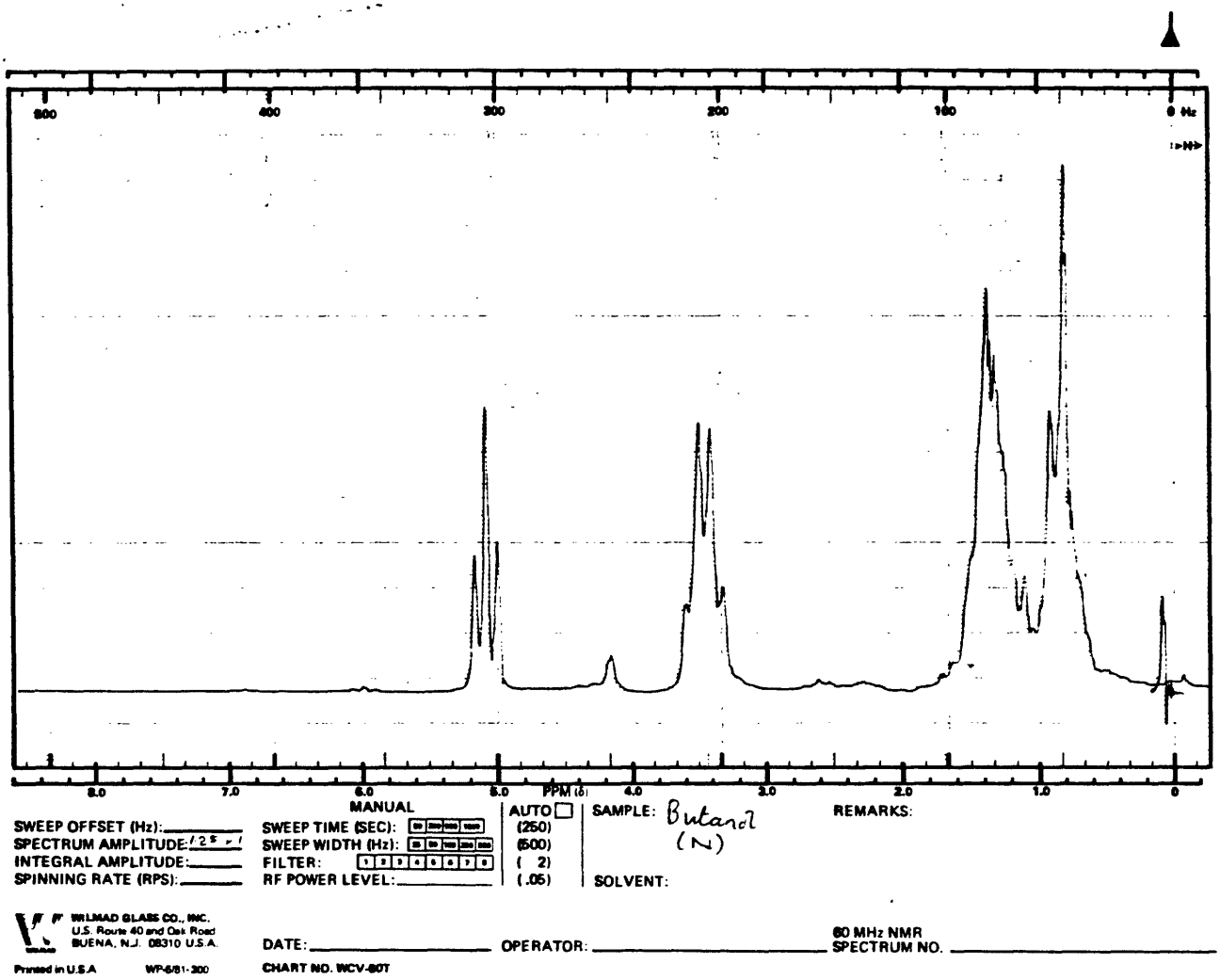

Figure 9. N-butanol spectra acquired using a 60 MHz dedicated CW NMR spectrometer. Sweep time was 250 seconds.

distilled water line indicates a frequency resolution of about 1 ppm for a 2.5 mm^3 voxel size, which is improved to about Ø.7 ppm for a 1.3 mm^3 voxel. The implication is that a significant amount of B_o heterogeneity over a given pixel arises due to z axis inhomogeneity. Most important however, the results of this experiment demonstrate the ability to perform chemical shift imaging across complex structures with diverse spectral characteristics. Although imaging time was quite long due to the long TR used in this data collection, in principle imaging times of objects with smaller T_1 can be made much shorter, especially if T_1 relaxation effects on signal intensity are accepted.

Bulk Magnetic Susceptibility Phantom: Background

When placed within a strong magnetic field, all materials have a magnetization induced upon them. This magnetization reflects the lining up of magnetic dipoles already present due to free, unpaired electrons (paramagnetic and ferromagnetic materials), or the induction of magnetic dipoles by the magnetic field's influence on electron pairs (diamagnetic substances). Normal tissue is diamagnetic, with an induced magnetic field about $1Ø^{-6}$ that of the applied static field. Para (and ferro) magnetic substances have a much greater interaction with the applied field, and hence the effect magnetic susceptibility might have on chemical

shift images can be documented using the large induced fields of a paramagnetic substance. This is additionally relevant because of efforts underway to utilize paramagnetic substances to enhance tissue contrast (paramagnetic contrast).

Results

The influence of magnetic susceptibility on the proton chemical shift is demonstrated graphically in Figure 10. Pulse sequence DELS was used for this scan, with TR = 500 msec, and 32x32 x and y phase encoding steps. These data were obtained from a phantom consisting of two coaxial test tubes with inside diameters of 10 mm and 30 mm. The outer annulus was filled with distilled water, and the inner tube contained a nickel chloride solution at a concentration of 0.16 M. Aqueous NiCl is highly paramagnetic at concentrations this large. Figure 10 shows edge profiles selected across a diameter of the phantom. In Figure 10a, the cylindrical axis was aligned parallel to the main magnetic field, B_o, while in Figure 10b, it was set transverse to B_o.

For the case of a long cylinder, the chemical shift of the protons within the paramagnetic solution is given to a first approximation by (59):

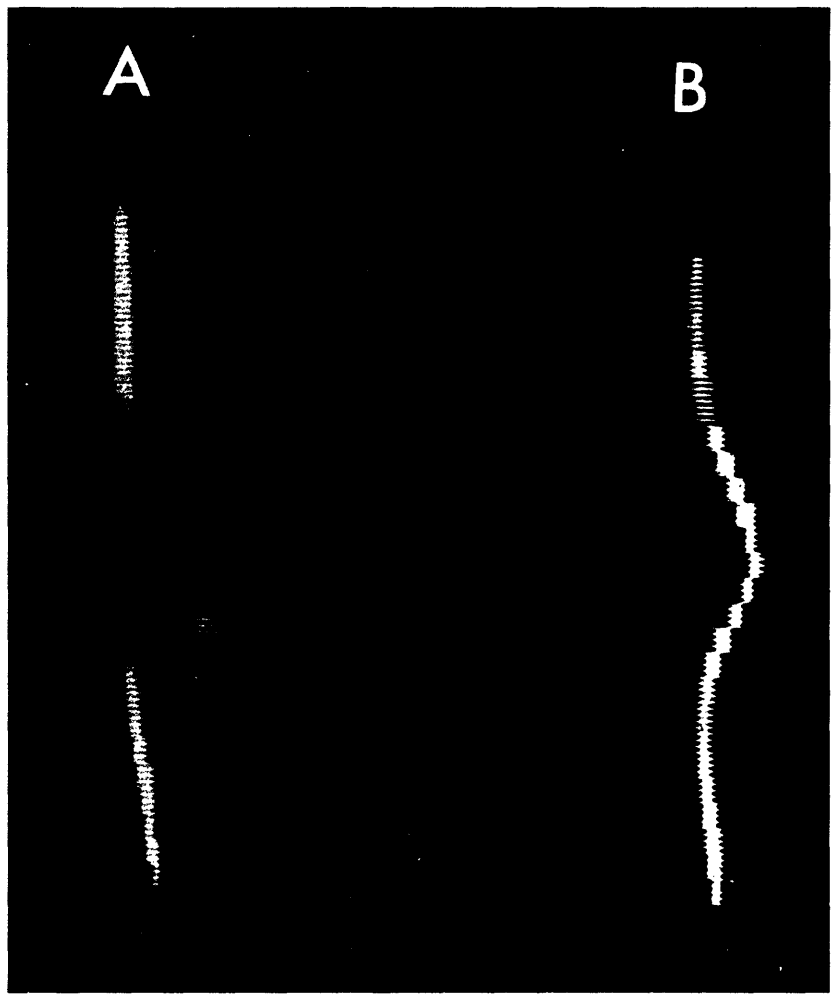

Figure 1Ø. Edge profiles extracted from the data matrix obtained from a coaxial test-tube phantom graphically demonstrate the influence of magnetic susceptibility on proton chemical shifts. The outer and inner tubes contained distilled water and Ø.16 M nickel chloride solution, respectively. Data obtained with the cylindrical axis of the phantom placed parallel to (a) and transverse to (b) the main field direction are presented.

$$\delta = (\frac{4\pi}{3} - \alpha) \quad \chi \times 10^{-6}$$

where χ is the volume magnetic susceptibility. With the cylinder parallel to the magnetic field, the demagnetization factor, α , is equal to zero, and the water within the inner, paramagnetic cylinder is shifted uniformly upfield. By measuring the frequency difference between the proton resonances of the pure water and the $NiCl_2$ solution, a value for χ may be determined. In the present experiment, a value for the mass susceptibility of nickel chloride, χ_m, of 38×10^{-6} was obtained; which is in good agreement (± 10%) with values quoted by others (60).

With the tubes placed transverse to the field, the magnetization induced by the paramagnetic solution becomes a more complicated function of geometry (61). This experimental approach provides a visual representation of this local time average magnetic field. The importance of these results to <u>in-vivo</u> studies of diamagnetic susceptibilities is discussed in Chapter V. In situations where high concentrations of paramagnetic materials are added for contrast, the possibility of measuring a susceptibility effect exists. Two factors will mitigate against this clinically. First, high concentrations of paramagnetic materials are in general highly toxic, and in fact important efforts are underway to enhance relaxation effects utilizing

very low concentrations of paramagnetic ions. Second, the effects are geometry dependent, hence accurate knowledge of the distribution of paramagnetic material is needed a priori to accurately assess the effect on chemical shift. Despite the potential clinical utility of magnetic susceptibility measurements (62), clinical measurement by chemical shift appears for now impractical.

Phantom Models: Discussion

The phantom data presented amply demonstrate the feasibility of performing chemical shift imaging by 3-D Fourier Transform methods on the MGH-Technicare prototype 1.44 tesla NMR imager. Spectral resolution better than 1 ppm is attainable, with slight improvements acquired by decreasing the z axis slice thickness. This increased resolution arises at the expense of S/N, however, with a 50% decrease in thickness in general requiring a 4x increase in imaging time to maintain the same S/N. In practical terms the need for spectral resolution will be balanced by time constraints. This is equally true of in-plane spatial resolution, for an increase of 2x in both spatial dimensions requires a 4x increase in the total number of phase encoded steps and hence imaging time, even if S/N is sacrificed 2x. This squared relation is the unfortunate consequence of phase encoding both spatial dimensions, and places a premium on

reducing spatial resolution to no more than that needed. This is an important limitation of the 3-D FT approach.

One possible way to avoid this dilemma is to perform the 3-D chemical shift experiment as outlined by Maudsley et al., where the frequency axis is phase encoded, and so one spatial axis can now quickly be frequency encoded. In this case the scan time is proportional to the first power, and not the square, of the number of spatial pixels along a line through the image. This technique is practical when the requirement for the number of points in the frequency spectrum is small (i.e., only a few peaks are present, and B_o inhomogeneity isn't large), and spatial resolution requirements are high. This experiment cannot be performed on the MGH imager, since phase encoding is controlled by gradient height, and not by time duration, as is needed to phase encode the resonance frequency spectrum. One other approach to high spatial resolution is discussed in Chapter VII, on solvent suppression techniques.

The ability to perform chemical shift imaging using both spin echo and "FID" (gradient refocusing) techniques permits important flexibility in designing <u>in-vivo</u> experiments, where T_2 relaxation times may be quite variable. In the case of spectral line components with relatively long T_2, the echo duration can be lengthened to allow T_2 effects to selectively enhance these lines. In the case of spectral peaks with

quite short T_2's, "FID" acquisitions will be necessary to assure that line intensity more nearly reflects only the spin density of these nuclei. In addition, the possibility that phase incoherence in FID techniques can be used to advantage to sensitively map out B_o field non-uniformities may in a sense compensate for the diminished spectral resolution of these scans. Furthermore, data have shown that if additional time between gradient switching and data acquisition is allowed, "FID" image quality can be improved significantly, an effect of allowing eddy currents induced by rapid gradient changes to diminish. Newer technology utilizing non-metallic magnet bores and more sophisticated gradient reversal methods should allow additional improvements in image quality with shorter TE delays.

Finally, the usefulness of using chemical shift imaging techniques as a research tool for field plotting is well demonstrated in the case of magnetic susceptibility. While using an NMR imager to measure paramagnetic ion concentration is certainly technologic overkill, the potential for interesting applications in materials science and clinical medicine is certainly present. The possibility that subtle susceptibility effects may be measurable <u>in-vivo</u> with more sensitive equipment opens the door to a new method of improving diagnostic specificity.

V. In-Vivo Models

In-Vivo Models

The goal of any diagnostic imaging examination is the discrimination and evaluation of pathologic tissues from normal structures in-vivo. Consequently, as a prelude to evaluating the potential of proton chemical shift techniques to study disease, the proton chemical shift imaging (PCSI) methods developed on non-living phantoms were tested on normal living systems.

Two in-vivo models were examined using PCSI; the human forearm and the cat head. The former was chosen for the convenience of having a cooperative and readily available subject, and due to the physical constraints limiting object size in humans to the upper extremity. The cat head was selected because the relatively large cortex provided a well-studied model for neurologic examination via NMR. As was the case with phantom models examined concurrently, considerable evolution in the preferred imaging parameters took place over time. Unlike the phantom models, additional constraints were placed on these examinations. For example, for both safety to anesthetized animals and comfort for human subjects, imaging time was limited to 45 minutes per examination. One benefit of this restraint was the enhanced relaxation time (T_1) contrast inherent in more rapid data acquisition using a spin echo pulse sequence. A second

priority placed more heavily on in-vivo exams was the removal to the largest extent possible of any imaging artifacts. This was necessary when viewing objects of unknown structure, to avoid misinterpretation of artifacts as new phenomena. As experience was gained the trade-off between image quality and the desire for new information can be made more readily. For example, data on spectral components with very short T_2 could be obtained at the expense of line broadening in the case of FID acquisition once the chemical shifts between native tissue protons were determined to be greater than the extent of the broadening.

Pulse Sequence and Image Parameters: Human Forearm

The pulse sequence developed for the in-vivo studies of the forearm was patterned after that used for the previous in-vitro data (DELS). The principal modification allotted additional gradient off time prior and subsequent to the 180° refocusing pulse, increasing the total TE time from 21 to 51 msec. The pulse sequence with this change is labeled DELL. This served two purposes. First, the degree of T_2 relaxation contrast is increased, important in light of the paucity of relaxation contrast in spin echo scans with short TR, and TE times of 20-30 msec (63). More important, by increasing TE, additional time is allotted for the decay of any small transverse magnetization component before data

acquisition begins. This is present after the refocusing pulse due to RF field inhomogeneities (non-180° pulse widths). This removes a potentially troubling artifact. Another approach to this problem is to include a significant amount of z axis gradient refocusing (post slice selection) after the 180° pulse. In this way residual transverse magnetization can be dephased along the z axis before data collection. This requires, however, that the gradient be fully switched off prior to data collection, or line broadening will result. The long TE time in DELL eliminated the need for this step. Placing the phase encoding gradients on after the 180° pulse (as done in DELS and DELL) will serve to spatially encode any signal from this pulse. While not removing this source of artifact, it will smear this signal over a broader region, eliminating a central point (x,y = 0,0) artifact derived from this effect.

The TR time used in imaging the forearm was 640 msec, and 64x64 phase encoded gradient steps were routinely acquired. In plane resolution was better than 2 mm. Imaging time was 45 minutes. Slice thickness was set to 1.5 mm FWHM, for a voxel size of 2.5 mm^3 (.0025 ml).

Results: Human Forearm

Figure 11 presents the results of a representative data set of a cross section through a forearm. Data in the figure

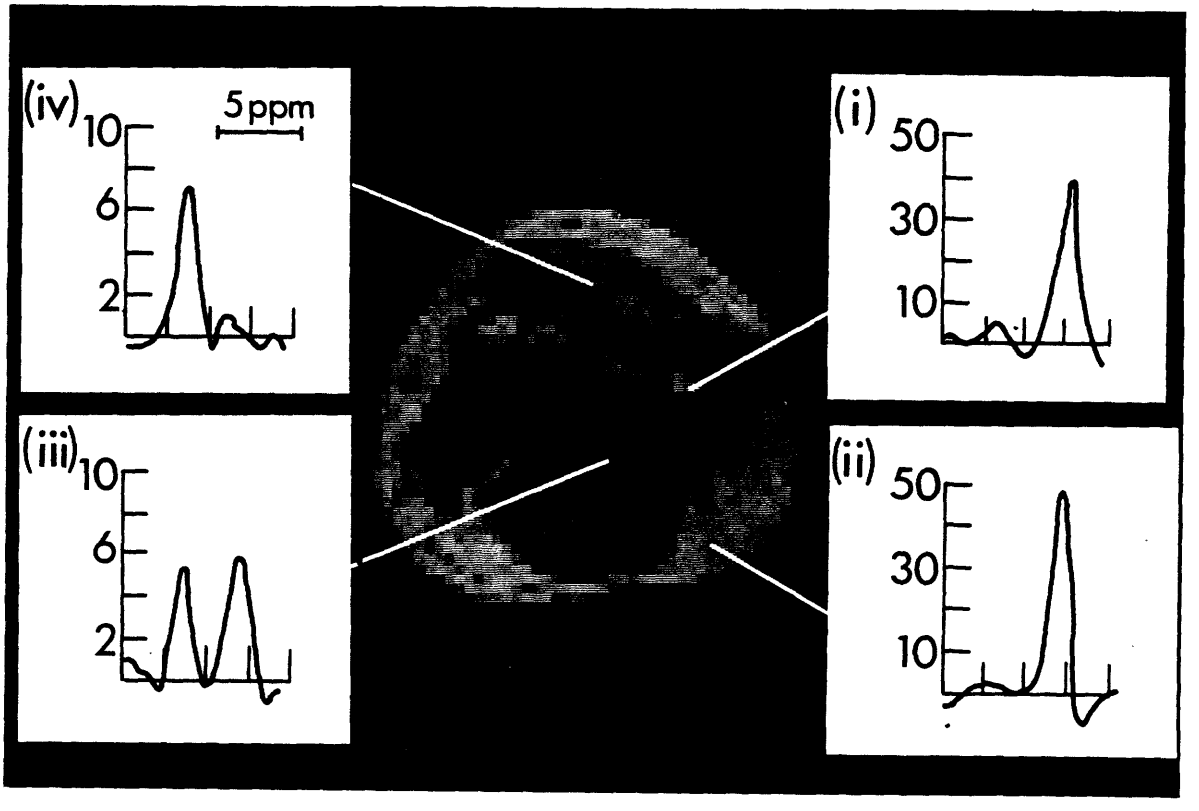

Figure 11. Data acquired <u>in-vivo</u> from a human forearm using a spin echo pulse sequence with TE = 51 msec. Total proton image is displayed centrally (integrated along ω), with NMR chemical shift spectra extracted from bone marrow (i), subcutaneous fat (ii), and muscle groups (iii, iv). Lipid signal is to the right. In (iii), the strong lipid signal is due to the presence of a fascial plane within the region of interest.

is represented in two fashions. Centrally, an integrated proton image is displayed. Here integration of signal intensity across all ω is carried out for each (x,y) point in the data matrix. Surrounding this image are four chemical shift spectra extracted from selected regions of interest. Four picture elements (2x2) were included within each region, thus spectral line width was modified by B_o inhomogeneity within these regions. The four areas chosen were muscle, subcutaneous fat, bone marrow, and muscle adjoining a fascial plane.

In all the human forearm studies, two separate chemical shift peaks were detected, separated by 3.7 ± Ø.3 ppm. By correlating these findings with <u>in-vivo</u> proton spectra of muscle (64) and with known samples of water and oil, these peaks were identified to correspond primarily with the resonances of water (H_2O) and long chain aliphatic lipid ($-CH_2-$) groups. Specifically, strong lipid signals are observed from regions of subcutaneous fat and bone marrow. The latter is normally fatty (non-erythropoetic) in the long bones of the upper extremity in adults. In addition, some lipid signal is seen within the muscle bundles of the forearm. However, the presence of a thin fascial plane containing fat separating muscle groups accounts for the large lipid response (seen in region iii in Figure 11) identified on these low resolution scans as muscle. In this

case, regions of both high fat and high water content were averaged together. The predominant signal from muscle is, of course, water.

Variations in the signal intensity of the integrated proton image are most significantly due to differences in the proton relaxation times of the muscle and lipid areas. (For comparison, a conventional NMR image through a forearm is shown in Chapter VII, Figure 22a). The short TR time used in acquiring this data introduces a significant degree of T_1 weighting into overall signal intensity. Spin echo acquisition leads to T_2 weighting as well. For these reasons, comparison of signal intensities will not in general lead to a measure of proton density. However, between regions where relaxation times are safely assumed to be constant, a relative measure of proton density can be made. The importance of this is highlighted in Chapter VI.

Cat Head

The growing importance of neurologic NMR examinations dictated that chemical shift imaging techniques be tested on studies of the brain. The largest cerebrum accessible within the 8 cm bore of the MGH magnet belongs to the cat, hence the choice of this animal model. While anatomic features such as facial musculature could also be studied. the predominant focus of this work was the brain. In particular, the

circumstances under which chemical shift data would provide biologically important data were closely studied.

Three principal investigations were carried out, with a total of nine imaging sessions on six animals. First, two preliminary studies were carried out with spin echo techniques similar to those previously discussed. Second, to address the question of myelin lipid, two additional studies were carried out with FID techniques (see Chapter IV) with short TE. Third, myelin membrane breakdown was investigated in a cerebral infarction model in two cats, over a total of five time points.

Cat Head: Spin Echo Acquisition Results

Figure 12a shows a representative integrated proton image obtained in an approximately coronal section through the head of a normal, anesthetized cat. The pulse sequence and image parameters were the same as in the previous forearm studies, with TE = 51 msec, TR = 640 msec. Spectra were investigated for a wide variety of tissues; for display are extracted four regions of interest, 2x2 pixels in size. In retro-orbital fat (i), a large lipid and smaller water peak is visible. The muscle of the tongue (ii) shows lipid and water in roughly equal proportions although, again, the peak heights are modified by the relaxation effects. The chemical shift difference was 3.6 $\pm$ .3 ppm. The region selected from the

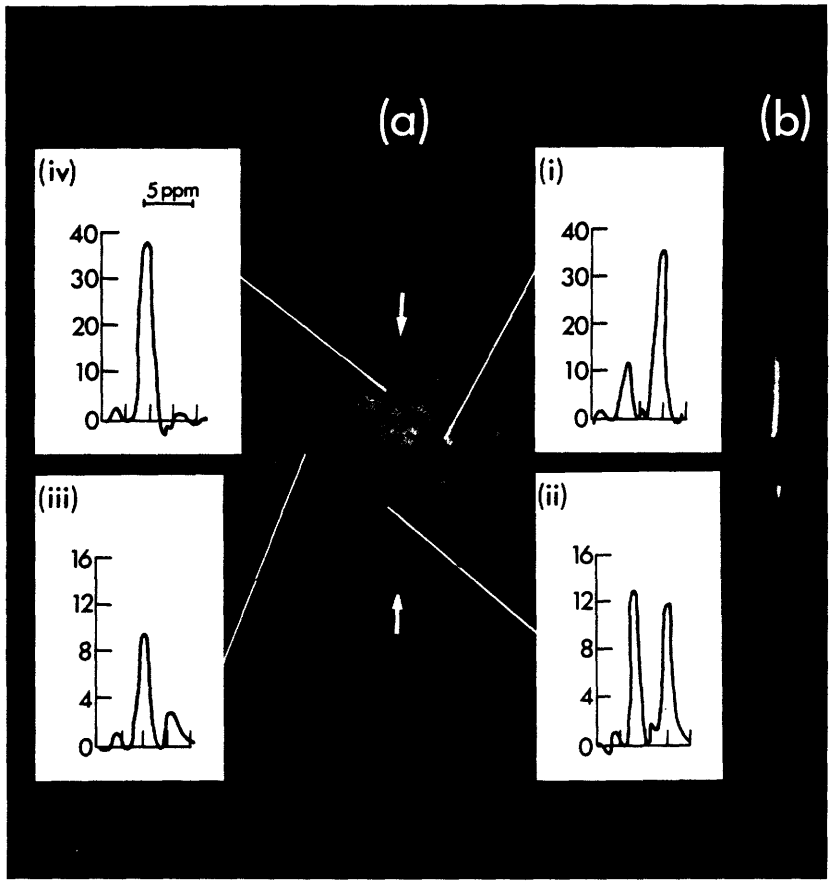

Figure 12. Data acquired using a spin echo pulse sequence with TE = 51 msec from a coronal section through the head of a normal, anesthetized cat. The integrated image shows the usual anatomical features, and NMR spectra from selected regions (i-iv) show clearly resolved peaks corresponding largely to water and to lipid resonances (a). An edge profile (b) taken through the head [location indicated by arrows in (a)] clearly shows both lipid and water resonances in the tongue, but only the water line is visible in the brain (lipid is to the left in this edge profile).

facial musculature (iii) shows a relatively low fat concentration. Of greatest importance, note that in the brain (iv), there is no lipid signal detected. This is seen more clearly in Figure 12b which shows an edge profile through the center of the head; there is a single water line through the brain, whereas two lines are observed in the region through the tongue.

This result was duplicated throughout the brain, in regions of both gray and white matter, and for both cats studied with spin echo techniques. Because it had been postulated that the different relaxation times in gray and white matter reflected differences in lipid content due to myelin concentration, the chemical shift response of brain in-vivo was further investigated.

Cat Head: FID Acquisition Results

In order to test whether the brain lipid protons with short T_2 relaxation times were present but invisible when using a long (51 msec) TE time, images of two normal cat heads were acquired using pulse sequence DELVS, which reads a gradient refocused signal with TE = 5 msec. (See Chapter IV.) TR was again set to 640 msec. As discussed, to eliminate phase artifacts, the magnitude of the reconstructed data set was displayed, resulting in some spectral line width broadening. Nevertheless, in no images were any lipid

signals visible above noise levels from regions of either gray or white matter. Representative total proton image and edge profiles are shown in Figure 13.

The lack of any lipid signal from the brain was at first puzzling, since the lipid/water weight ratio in white matter is Ø.22 (.Ø8 in gray matter), a substantial fraction (65). Unlike in muscle or subcutaneous fat however, lipid present in the brain is in the form of membranes rather than free lipid droplets. For example, in white matter, the high lipid content is due primarily to myelin sheath membranes. Spectroscopic studies in intact rat muscle (64) and more recently in in-vivo spectroscopy of the rat brain (15) failed to demonstrate substantial signal from membrane lipids. In-vitro studies of dog brain using a 6Ø MHz CW spectrometer at the MGH corroborate these data. The difference is postulated to lie in the mobility of the protons studied; in membranes (as in solids) the highly ordered lattice leads to very short T_2 relaxation time with accompanying broadening of the spectral line width, while depot lipids in muscle or adipose are freely mobile with longer T_2 time and thus narrow spectral widths (64).

Cat Head: Cerebral Stroke Model

One consequence of the above result is that disruption of normal membrane structures in brain may lead to visible lipid

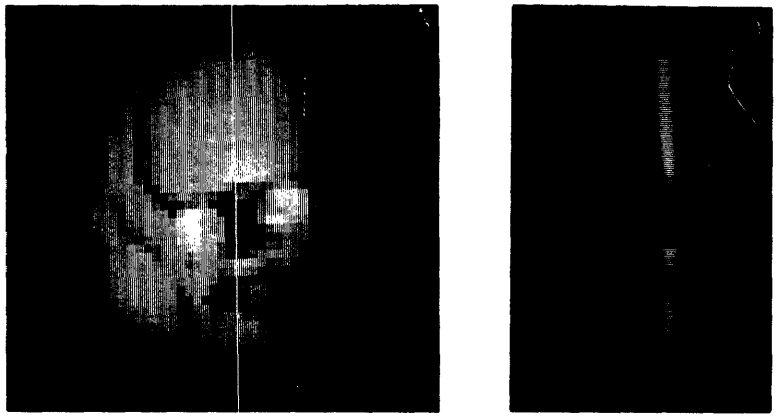

Figure 13. Data acquired using an "FID" pulse sequence with TE = 5 msec from a coronal section through the head of a normal, anesthetized cat. On the left is an integrated proton image, on the right an edge profile through the region of the brain (along the line shown). No clear lipid signal is seen in any regions of the brain.

signals from regions otherwise dominated by water signal. The appearance of lipid signal in sonicated erythrocyte membranes (66) points to this possibility. One circumstance where this disruption takes place to a certain extent is within infarcted tissue, where clearing and processing of dead tissue by macrophages leads to the presence of lipid droplets within a contracting rim around the infarct. To investigate this process chemical shift images were acquired of two cat heads with cerebral infarcts, produced by occluding the middle cerebral artery by a snare ligature technique. A total of five imaging sessions were obtained from 10 days to 5 weeks post infarct, spanning the period of active tissue breakdown. Pulse sequence DELL was used. anticipating lengthened T_2 relaxation times from free lipid released by membrane destruction. Sequence parameters were as for Figures 11 and 12.

Representative results are shown in Figure 14. Unfortunately, in no circumstances were any lipid signals clearly detected. The reasons for this are probably two-fold. First, the rim of fat filled macrophages is usually quite narrow (67), leading to partial volume effects within the relatively large pixel size used for these chemical shift studies. Second, the concentration of fat is at most still much smaller than fatty tissue such as adipose. Together, the overall sensitivity to membrane breakdown is

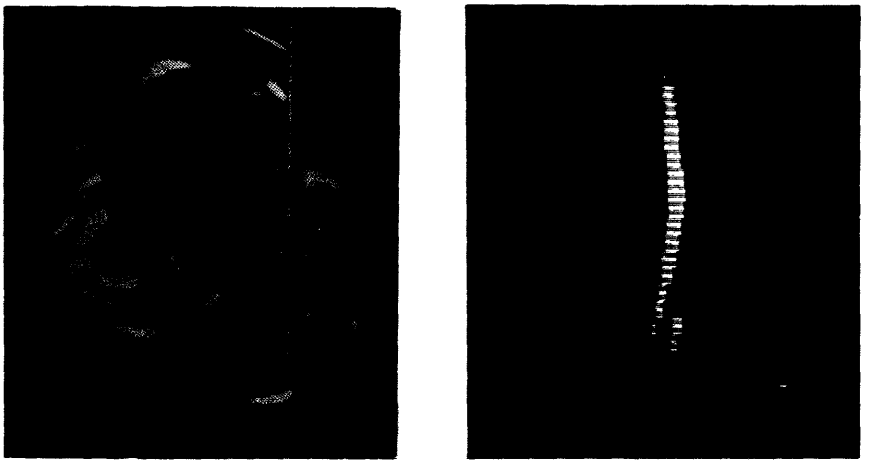

Figure 14. Data acquired using a spin echo pulse sequence (DELL) from a coronal section through the head of a cat with a 14 day old infarct. On the left is a conventional "2-D" NMR image acquired using an inversion-recovery (T_1 weighted) pulse sequence (TI = 400 msec). The region of the infarct shows up dark, corresponding to a longer T_1 (upper third of the brain on this image). On the right is an edge profile through the region of the brain (along the line shown). No clear lipid signal is seen within the brain. Subcutaneous fat is seen at the top and bottom. The lack of gray-white contrast on the edge profile data is due to the different pulse sequence used for the chemical shift versus conventional image.

expected to be low. Higher resolution scanning (for example, using the techniques of Chapter VII) and additional signal averaging may help correct these problems. The addition of in-vitro studies of infarcted cerebral tissue using high sensitivity NMR spectrometers would help elucidate whether chemical shift analysis offers hope of more specifically characterizing brain lesions.

Cat Head: In-Vivo Magnetic Susceptibility

As discussed in Chapter IV, bulk magnetic susceptibility can influence the resonance frequency measured in a chemical shift experiment. Although diamagnetic mass susceptibilities of tissues are small (~ 0.7×10^{-6} emu/gm), and variations between both normal and pathologic tissues smaller (68), the complex geometry of living organisms makes predicting the exact amount of frequency offset difficult. Understanding the magnitude of these effects is important for two reasons. First, susceptibility shifts on the size scale of one voxel will lead to line broadening of spectral features within those voxels. Second and more important, large susceptibility shifts, even if gradual over an extended region, will mean that B_o cannot in general be shimmed across an extended object. While this is not crucial for the chemical shift studies outlined above (which require adequate B_o homogeneity over voxel dimensions only), application of

techniques such as solvent suppression to eliminate the water proton signal becomes problematic with large B_o heterogeneity. (This is discussed in more detail in Chapter VII.)

Data were acquired on the previously described cat stroke model to assess magnetic susceptibility effects in-vivo. Using pulse sequence DELL, a longitudinally oriented cylindrical bottle of water was imaged (length/diameter = 5/1); sequence parameters were as for Figure 14. The water resonance frequency was adjusted to on average coincide with the water line of a similar chemical shift data set acquired from a coronal section through the head of an infarcted cat (4 weeks post-infarct). Because the susceptibility shifts within a longitudinally placed cylinder are uniform across a transverse plane (59), curvature in the edge profile data from this phantom reflects B_o heterogeneity and not susceptibility effects. Edge profiles from both the cylindrical phantom and the cat head could then be compared for correspondence; the smaller any in-vivo susceptibility variations were, the better the expected alignment of edge profiles from the same region within the magnet. Similarly any large in-vivo susceptibility shifts would be manifested by a divergence of the in-vivo edge profile data from that of the uniform phantom.

Representative results of this analysis are shown in Figure 15. In all edge profiles examined (n = 7, spanning

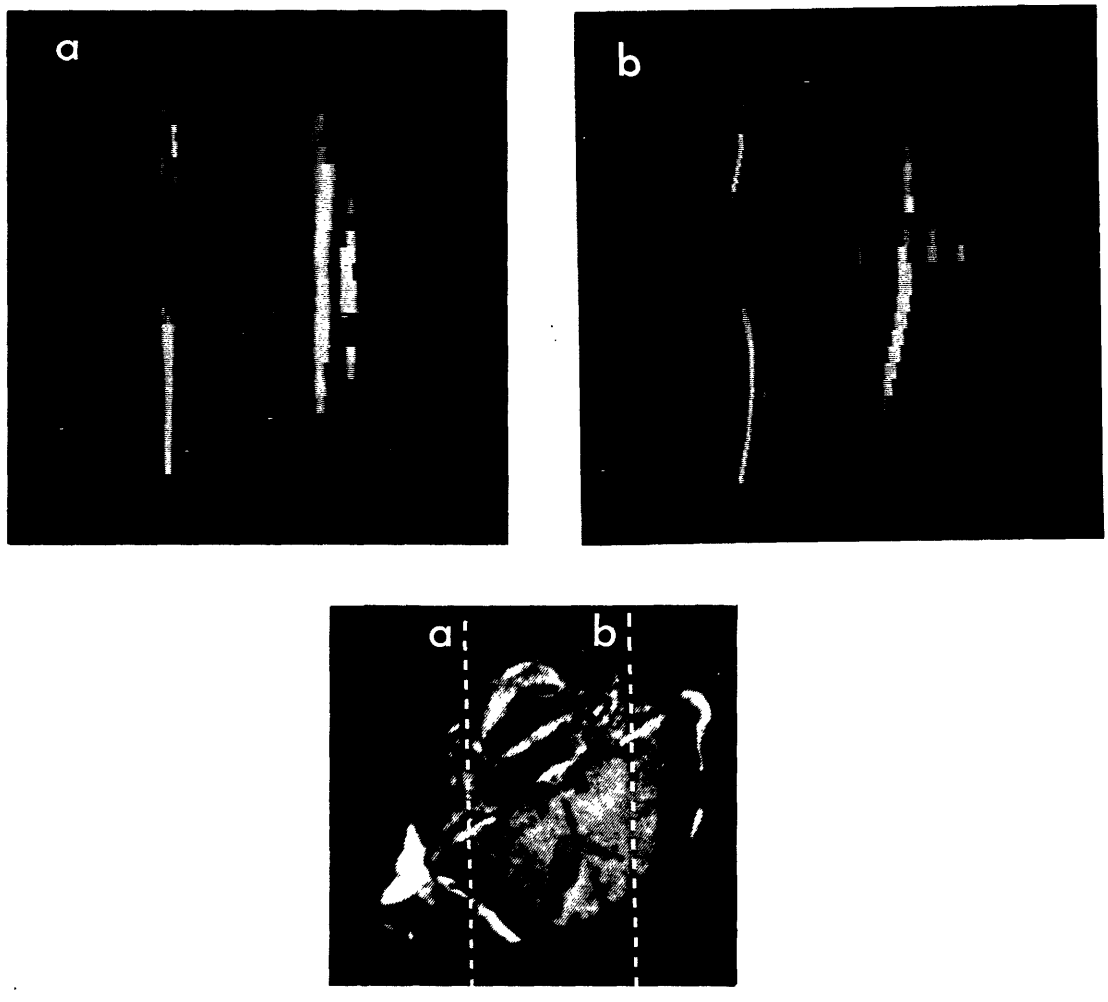

Figure 15. Edge profile data is displayed from two regions within a cat head, as well as from the same region within a cylindrical water phantom oriented longitudinally with B_o. For each region (a and b) the cat head edge profile is displayed above the corresponding phantom edge profile on the left. On the right is an expanded view of the sum of these two images. Note that in no case are two distinct lines visible from the water profile in this summated image, reflecting magnetic susceptibility effects less than 1 ppm. Regions of fat appear in the cat head and summated profiles to the right. An inversion recovery image through the same slice, with the corresponding edge profile lines (a and b) is shown below.

the extent of the cat head) the correspondence between edge profile images from the two data sets was quite good. In no cases were two distinct water lines seen on summated images (superimposed edge profile images from the cat head and water phantom, corresponding to the same region within the magnet). Given line widths of about 1 ppm, this implies that non-uniform magnetic susceptibility shifts in-vivo were less than 1 ppm in this animal model. Across the region of the cat brain, including the region of the infarct, the correspondence was better than Ø.5 ppm. Even across discontinuous regions such as the oral pharynx, no larger shifts were seen. Of course, these data can demonstrate only variations in magnetic susceptibility shifts, and will be insensitive to any superimposed constant shift.

Although these experiments will need to be repeated, particularly in humans, the results are not unexpected. Because the head of the cat (and human as well) is approximately spherical, and the demagnetization factor within a sphere is such that no magnetic susceptibility shifts are seen (59), to first order magnetic susceptibility should not influence resonance frequency within the head. The same should hold true of any organ approximated by a sphere (e.g., the heart), as well as any cylindrically shaped region, such as an arm or leg, for reasons discussed earlier. This latter point, however, requires that different tissues

have similar susceptibilities. This is true for normal soft tissues. The fact that susceptibility variations are small in the brain, even in the presence of a massive infarct, is encouraging for application of solvent suppression techniques to study low concentration metabolites.

In-Vivo Models: Summary

The data presented here amply demonstrate the feasibility of in-vivo proton chemical shift imaging, even using a magnet not specifically designed for this purpose. In biological tissue, proton spectra consist typically of two relatively broad peaks corresponding to the resonances of water and aliphatic lipid groups. Specifically, strong lipid signals are observed from lipids in subcutaneous fat and bone marrow. The lipid resonance seen from muscle originates from depot lipid and nearby fascial planes since intact muscle membrane lipids do not give any appreciable NMR signal. This fact would be of use in allowing PCSI to monitor lipid energy stores during muscular contraction (64).

An important observation of the experiments on the cat brain was that no lipid signal was observed from the brain. The discrimination between gray and white matter tissue observed on clinical NMR head images is probably due to environmental modifications of water proton relaxation times, rather than to direct observation of myelin lipid protons per

se. With additional technical refinement, this fact may be used to advantage in specifically recognizing pathologic tissue (infarcts, demyelinated plaques) on the basis of the presence of a lipid component to their NMR signals.

Bulk susceptibility measurements in the cat head show that variations less than 1 ppm are observed. This is true despite the presence of significant pathology. An important application of this finding is that, with proper shimming, magnetic field homogeneity can be made good enough to perform useful spectroscopy (1 ppm line widths) over very large areas. This will be important for applications of solvent suppression techniques discussed in Chapter VII.

VI. Proton Chemical Shift Imaging Evaluation of Fatty Liver Change in Rats

Fatty Liver Change: Study Criteria

Having demonstrated the capability of chemical shift imaging to detect tissue water and lipid proton in-vivo, a disease model was sought which would test the ability of these techniques to discriminate normal from pathologic tissue. A number of criteria were set in choosing an appropriate model for study. First, a simple animal model for the disease should exist, well-studied and with established in-vitro biochemical correlation. Second, the model should include a wide range of disease responses, to allow for the evaluation of sensitivity in detecting pathology. Third and most important, the disease model should have as a primary tissue characteristic a significant change in total fat content, the chemical group most easily distinguished from the predominant tissue water signal by proton chemical shift imaging. Further criteria would include a disease which in humans is not well studied by other non-invasive modalities, and one with clear importance to human pathology although both of these would be less important in any first attempt study.

Fortunately, a single disease model, fatty liver change in the rat, met all of these criteria reasonably well.

Fatty change, the accumulation of triglyceride within hepatocytes, is a generalized response by the liver either to significant injury or to systemic disorders of fat mobilization or metabolism, and in humans occurs in a number of diseases, including diabetes mellitus, tuberculosis, Reye's syndrome in children, and chronic alcoholism (69). Because fatty change is a reversible process often associated with hepatomegaly, the ability to distinguish it from other causes of liver enlargement can be of great clinical importance (69). Although xenon radionuclide studies can give a qualitative measure of hepatic steatosis (70) and percutaneous liver biopsy a definite one, the hazards (71) and uncertainties associated with these exams makes a quantitative, non-invasive method for characterizing liver lipid infiltration desirable.

Good animal models also exist for fatty liver disease. Fatty change is easily induced in rats by a number of chemical challenges, including agents known to produce similar changes in humans. Furthermore, the range of fatty buildup is quite variable, and can be measured <u>in-vitro</u> by biochemical assays for triglyceride content, the major component of lipid deposits in the liver. One additional advantage; in fatty liver syndrome, conventional ^{1}H NMR imaging failed to differentiate chemically induced fatty change from normal livers in rats (72), thus it appears

conventional NMR imaging is limited in its ability to characterize this lesion.

Spectroscopic NMR studies have not shown this limitation. In-vitro studies of fatty liver change, using ^{13}C and ^{1}H NMR spectroscopy, have shown elevations in $-CH_2-$ aliphatic groups consistent with increased liver triglycerides (73). In-vivo spectroscopic techniques, such as surface coil and topical magnetic resonance (19,22,74), will allow for the extraction of NMR spectra from intact tissues. However, both techniques currently suffer from inaccurate spatial localization and consequent contamination of the signal by adjacent structures such as subcutaneous fat. This would interfere with efforts to quantitate the degree of fatty response in liver tissue using these techniques. Chemical shift imaging, by allowing for the acquisition of NMR chemical shift spectral information from each picture element in a ^{1}H NMR image, avoids this complication. Using this non-invasive technique, this chapter reports on the in-vivo detection and quantification of fatty change in rat livers.

Fatty Liver Models: L-Ethionine and Ethanol

Fatty liver change was induced in nine female rats using L-ethionine. The fatty liver resulting from ethionine treatment has been shown to be related to its antimetabolic properties. It depletes hepatic ATP content which leads to

inhibition of protein synthesis. Deficient synthesis of apoprotein of the VLDL required for movement of triglyceride from the liver leads to the fatty liver. There is minimal necrosis by the ethionine treatment (75). The L-ethionine dose was 1 g/kg, administered via a single intraperitoneal injection, 25 mg/ml in water. Fatty change was also induced in seven female rats using ethanol. The fatty liver resulting from acute ethanol ingestion has been shown to be caused by the mobilization of adipose tissue fatty acids, increased triglyceride synthesis, decreased triglyceride release, and decreased fatty acid oxidation. This model also produces steotosis but no necrosis (76). The ethanol dose (50% volume/volume in water) was varied between 7.5 to 9.3 gm/kg in order to stimulate a wide range of fatty response. Administration was by gavage. Two control animals received a small dose of glucose orally, isocaloric with the high ethanol dose. All animals were subsequently fasted with water ad lib, and imaged 18 hours later. After imaging, animals were sacrificed and liver triglyceride content obtained following Folch extraction and thin layer chromatographic separation (77).

Pulse Sequence and Imaging Protocol

Chemical shift data sets were acquired using pulse sequence DELL (see Chapter V). TE time for this sequence was

fixed at 51 msec. The slice thickness was increased 3x over previous studies to 5 mm, providing increased S/N in detecting low concentrations of fat. This was accomplished by decreasing the z-axis gradient on during phase selection.

The imaging protocol consisted of first locating the desired transverse image plane using conventional 2-D NMR imaging. The technique used for these images consisted of a spin echo sequence, with TR = 200 msec and TE = 30 msec. This sequence is described in greater detail in the Appendix. Subsequently, chemical shift imaging was performed through the same slice with 32 x 32 picture elements in the image plane (in plane resolution = 2.5 mm), and 256 points acquired along the chemical shift axis (0.26 ppm/point). This is a decrease of a factor of 2x in spatial resolution, performed in order to decrease the average imaging time. With two signal averages and pulse repetition rate, TR, of 149 msec, imaging time was approximately six minutes.

In order to permit computation of the spin-lattice relaxation time (T_1) for each constituent peak in the proton NMR spectra, for two rats (one ethanol and one L-ethionine) chemical shift images were obtained using four different TR intervals; 149, 245, 605, and 905 msec. With two signal averages for each time point the total imaging time was 1 hour 10 minutes.

Results

Representative images from a control and an L-ethionine treated rat are shown in Figure 16. In the control animals only a single spectral component is visible in the region of the liver, corresponding to H_2O protons. Lipid ($-CH_2-$) proton signal was confined to regions of subcutaneous fat. Liver triglycerides in the control animals were <4 mg/gm wet weight. In the L-ethionine and ethanol rats with significant triglyceride content elevations, an additional spectral component, corresponding to $-CH_2-$ aliphatic protons, was clearly visible within the liver.

The aliphatic signal intensity from chemical shift picture elements within the liver was measured, and compared to the triglyceride levels determined by biochemical analysis of the excised livers. Because of the coarse spatial resolution of the chemical shift images, determining the extent of the liver directly from them was problematic. For this purpose correlation of spatial (x,y) coordinates with the higher resolution conventional NMR image was most useful. To avoid measuring regions of subcutaneous fat or muscle, only the central 50% of the liver area was used for aliphatic signal intensity measurements. Measurements were made by integrating over the lipid spectral profile using a region of interest cursor. The results of this analysis are shown in Figure 17. There was excellent agreement between the liver

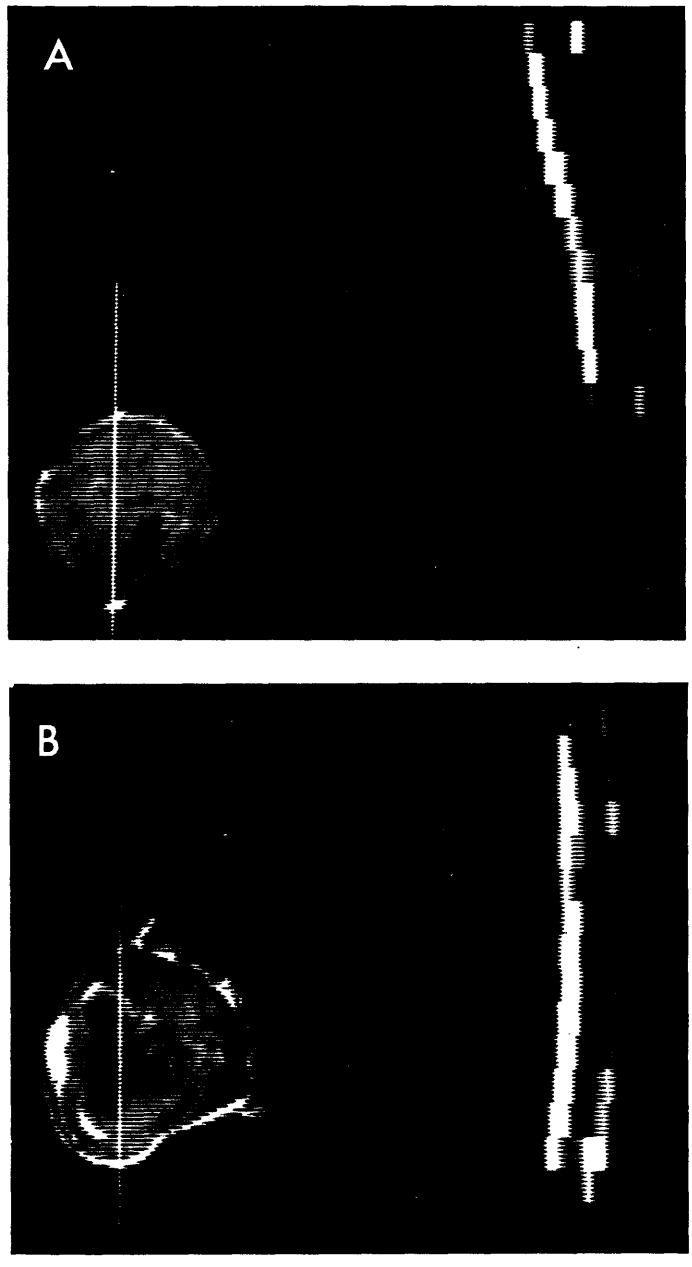

Figure 16. Representative data from normal (a) and L-ethionine treated (b) rats. The left side of each image displays the conventional 2-D NMR image (spin echo technique, TE = 30 msec, TR = 300 msec) through the mid portion of the liver. The signal intensity of the liver is not significantly different between normal and treated animals. To the right of each conventional image a single edge profile is displayed. Vertical position corresponds to the vertical line drawn through the liver of the 2-D image. In the normal there is one resonance line through the region of the liver, representing water protons. Shifted to the right at the top and bottom are $-CH_2-$ lipid protons from regions of subcutaneous fat. In the L-ethionine treated rat both water and lipid resonance peaks are now clearly visible through the region of the liver.

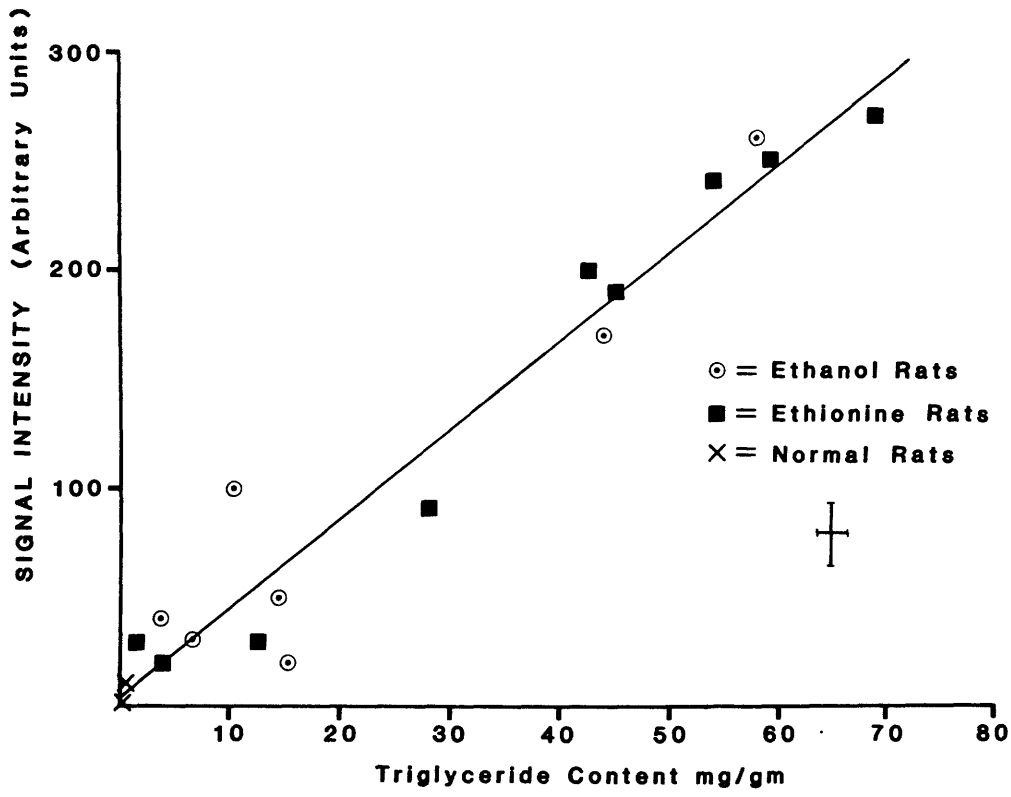

Figure 17. Liver triglyceride content (mg/gm wet weight) plotted versus aliphatic proton signal intensity from chemical shift imaging measurements within the liver. An overall correlation of r = .97 was determined. 1σ error bars are shown in lower right.

triglyceride content and aliphatic signal intensity ($r = .97$). The NMR lipid signal intensity visible on these seven minute images closely reflected the wide range of triglyceride values present in these test animals. Using the imaging parameters discussed, proton chemical shift imaging appears to be sensitive to triglyceride concentrations of >10-20 mg/gm wet weight, or about 1-2% lipid content. The observed non-uniformities in the lobar distribution of fatty infiltration with ethanol fed rats (coupled with incomplete sampling of the total liver volume), small variations in aliphatic relaxation times, and variations in the (triglyceride)/(total lipid) ratio would all introduce scatter into Figure 17. The more uniform distribution of fat within ethionine treated animals significantly reduced the degree of scatter observed for these animals. This implies that chemical shift imaging is probably quite accurate in assessing fat content on a pixel by pixel basis, and that other effects such as changes in aliphatic relaxation times are likely small.

Data from two treated animals were acquired at the four values of TR. Chemical shift spectra were extracted from a small (0.125 cc) volume within the liver of these animals for each TR tested (Figure 18). From these data, T_1 relaxation times were calculated separately for the water and lipid protons using the methods outlined in the Appendix. The

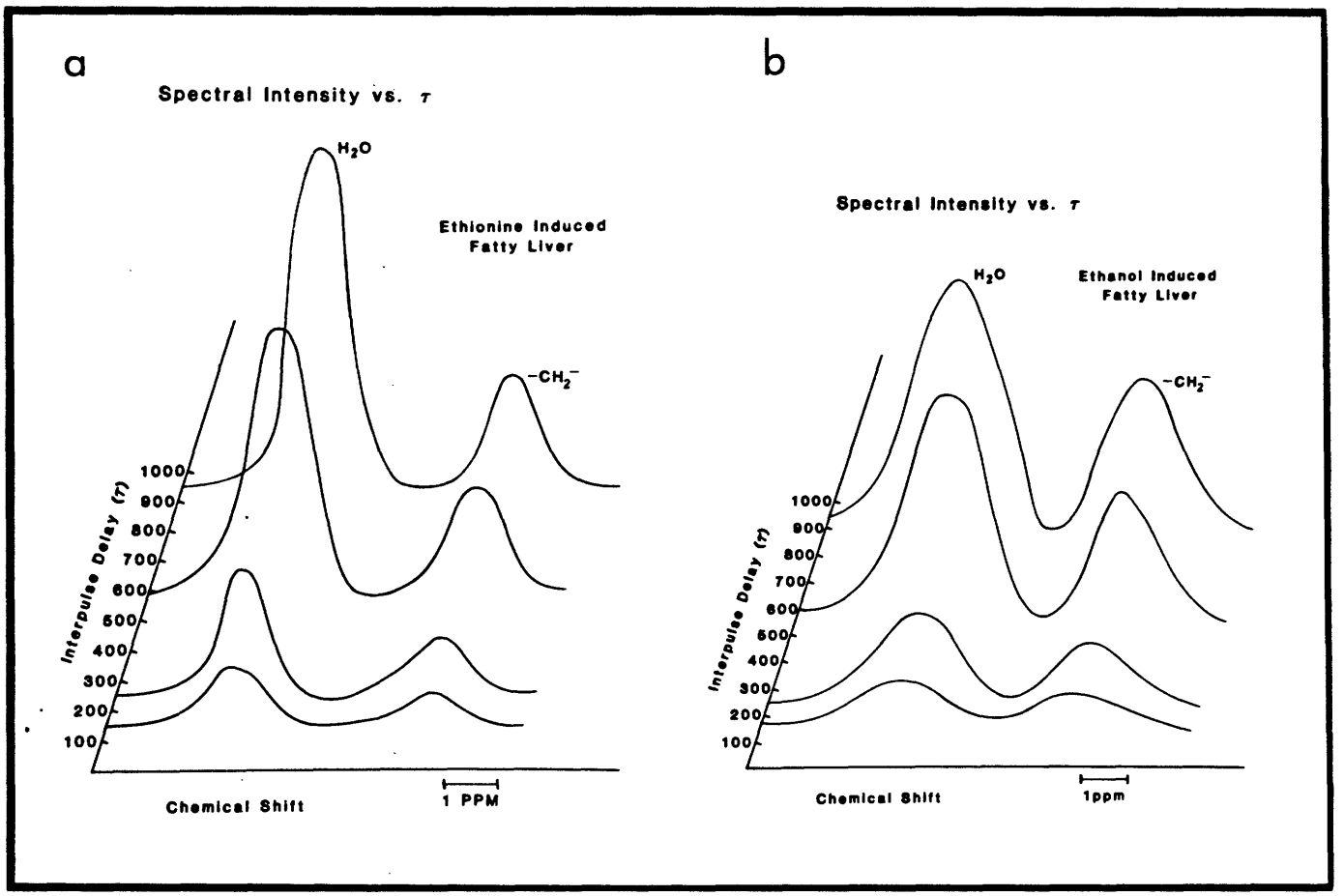

Figure 18. Four chemical shift spectra extracted using chemical shift imaging from a small volume (.125 cc) within the liver of an L-ethionine treated rat (a) and ethanol treated rat (b); TR values of 149, 245, 605, 965 msec were used. Lipid peak is to the right of the water peak. Integrated lipid and water peak intensities at each value of TR formed the basis of T_1 relaxation measurements.

results were as follows:

	T_1 (H_2O)	T_1 (Lipid)	Triglyceride (mg/gm)
L-Ethionine:	490	350	70
Ethanol:	500	320	30

All T_1 are in milliseconds. Measurement error is estimated to be within 10%. An average T_1 difference of 160 msec was measured, confirming the multi-exponential relaxation behavior of tissues with non-exchanging proton populations. As expected, the relaxation times of the aliphatic protons were not strongly dependent on their proton concentrations (as reflected by triglyceride content), and were in fact quite similar in the two drug models which both produce fatty change without tissue necrosis. This is because fat appears as compartmentalized lipid droplets within fatty livers; as triglyceride concentration increases, the number of lipid droplets increases, without a change in their character (69).

Fatty Liver Model: Discussion

By acquiring spectral data within a true imaging context, chemical shift imaging allows for a quantitative, non-invasive, in-vivo measure of fatty change in rat livers. This provides a valuable analytic tool in the laboratory investigation of factors modifying fatty liver disease.

Perhaps more important, these methods offer the promise of improved diagnostic accuracy and safety in the clinical evaluation of fatty change in humans, since both percutaneous biopsy and radionuclide exposure may be avoided. In general, it should be possible to correlate relative measurements of signal intensity with quantitative measures of lipid content. The use of reference standards with known fat content, which can be included within the plane of each image acquired, would facilitate this. Variations in lipid relaxation times would modify any correlation, although for the reasons already given this should in fact not be problematic.

Chemical shift imaging also promises a further degree of tissue characterization not obtainable with other non-invasive measures of fatty liver. Because water relaxation times are elevated in the liver when inflammation or necrosis is present (72,78), acquiring independent relaxation times for lipid and water components may allow tissue necrosis to be measured independent of the degree of fatty infiltration. This is important because variation in lipid content found in diseased tissue will modify the measurement of average (water and lipid) relaxation times made using conventional NMR imaging, and is seen as follows. To first approximation, the measured T_1 of two non-exchanging proton populations is the weighted mean of the individual protons (this is true so long as the T_1 difference is not too

large). For example, a disease process characterized by an elevation of water T_1 from 500 msec to 600 msec, along with an increase in fat content to 10%, will decrease the average T_1 change by over 30% when compared to water T_1 measurement (fat T_1 assumed to be 330 msec).

The results of these experiments show quite convincingly that proton chemical shift imaging can obtain information of potential value to clinicians in reasonable times and with resolution similar to that in nuclear medicine studies. The ability to obtain high resolution conventional NMR images for spatial registration may in many circumstances make higher resolution unnecessary. Further studies, such as those investigating the ability to measure necrosis via changes in water T_1, are currently being carried out on a collaborative basis with other investigators at the MGH and elsewhere. The ultimate role that studies of this kind may have on clinical medicine is not clear; the final chapter of this thesis discusses some of the important considerations addressed by this question.

VII. Selective Saturation Proton NMR Imaging

Introduction

Techniques outlined thus far in this thesis allow for acquisition of NMR chemical shift data *in-vivo* within a proton imaging context. Although primitive by spectroscopic standards, these studies have successfully demonstrated the ability to visualize lipid and water containing regions in both normal and pathologic states *in-vivo*.

Over the last several decades, however, NMR spectroscopists have developed a number of sophisticated techniques to extend the versatility and usefulness of NMR studies. Some of these, such as sample spinning to reduce B_o inhomogeneity effects, are (obviously!) impractical for *in-vivo* NMR imaging. Others, for example Waugh pulse sequences for the study of solids (79), are not necessary for investigating the fluid compartments of biological tissues. However, a few of these more advanced methods may become important for the NMR imager. This chapter will focus on one of these, selective saturation or solvent suppression, and discuss two areas where NMR imaging can use these techniques; the first in a sense familiar to spectroscopists allowing for visualization of dilute chemical moieties such as intracellular lactate (however now within a proton chemical shift image), the second a new application to facilitate

chemical shift contrast in conventional NMR imaging.

Selective Saturation in Proton Chemical Shift Imaging

Using proton chemical shift imaging, data presented in previous chapters have demonstrated the ability to obtain NMR spectral data from all pixels within an NMR image of complex phantoms, with frequency resolution better than 1 ppm and spatial resolution approaching 1 mm. In-vivo the water resonance dominates in most soft tissue, such as brain and muscle, with only aliphatic CH_2 protons from fatty tissues having sufficiently high concentrations to contribute to the measured chemical shift spectra. However, within biologic tissues many distinct chemical moieties exist at lower concentrations (<50 mM) which have well identified proton resonance spectra. Studies of the brain, for example, have demonstrated via proton NMR spectroscopy increasing tissue lactate concentration with hypoxic stress (16). The key to performing studies such as these is the need to suppress the overwhelming water signal, to overcome dynamic range and digitization problems. This selective saturation is in general accomplished by rotating the spins of the unwanted water protons in such a way that they have no net transverse components during the signal acquisition phase of an NMR experiment and thus produce no signal. A number of techniques, using both long (narrow bandwidth) and hard

(broadband) pulse methods, have been developed to accomplish this in the NMR spectrometer (80-82). Discussed below is the application of a simple selective saturation method within an imaging context, which allows the visualization of lactate concentrations in the pathophysiologic range in phantoms.

Selective Saturation: Pulse Sequence and Image Parameters

All studies reported here were acquired using the prototype 8 cm bore Technicare NMR imaging system operating at 61 MHz (1.4 tesla) (Chapter III). The imaging method used modified the chemical shift imaging techniques discussed previously, by adding a single preparatory saturating pulse just prior to plane selection. Selective saturation is achieved by the application of a narrow bandwidth 90^{o} selective pulse applied in the absence of any magnetic field gradients. Following this preparatory pulse, plane selection and refocusing pulses are applied in a manner discussed earlier, allowing for spin echo data acquisition. Because the T_2 of lactate is long (~ 150 msec) and because of the effect of homonuclear spin-spin coupling on the spin echo amplitude of lactate's terminal CH_3 protons (34), the time to echo, TE, was increased to 136 msec. This lengthened TE allows for the entire spin echo to be read, centered within the data collection period. A strong z-axis spoiler gradient is applied after the saturating pulse, which is used to

dephase any residual transverse magnetization from this pulse prior to plane selection. To diminish noise and artifacts arising from cutoff of signal in the time domain, 1024 data points are collected and sampled every 120 μsec, increasing the total data collection time by 2x over the previously described sequences. Figure 19 schematically demonstrates the selective saturation pulse sequence.

In order to demonstrate the feasibility of applying this technique to form images of dilute chemical substrates, a series of imaging experiments on aqueous lactate phantoms was performed. Lactate was chosen for its importance as a metabolite of tissue under anoxic/ischemic stress. In these experiments, spatial resolution was 2.6 mm (32 x 32 pixels across the 8 cm bore), with a slice thickness of 6 mm (FWHM). Imaging time was 53 minutes, with 8 signal averages per projection and a pulse repetition rate, TR, of 360 msec. Serial dilutions in lactate concentration from 160 mM to 40 mM were tested, both with and without H_2O saturation. Because of B_o non-uniformities in the image plane, only a single 2 cm diameter phantom could be imaged at a time when using solvent suppression, since the technique requires homogeneity of approximately 2 ppm across the entire imaged region. Inhomogeneities greater than this would imply the need for a broader frequency saturating pulse, which would then compromise the equilibrium magnetization of the lactate

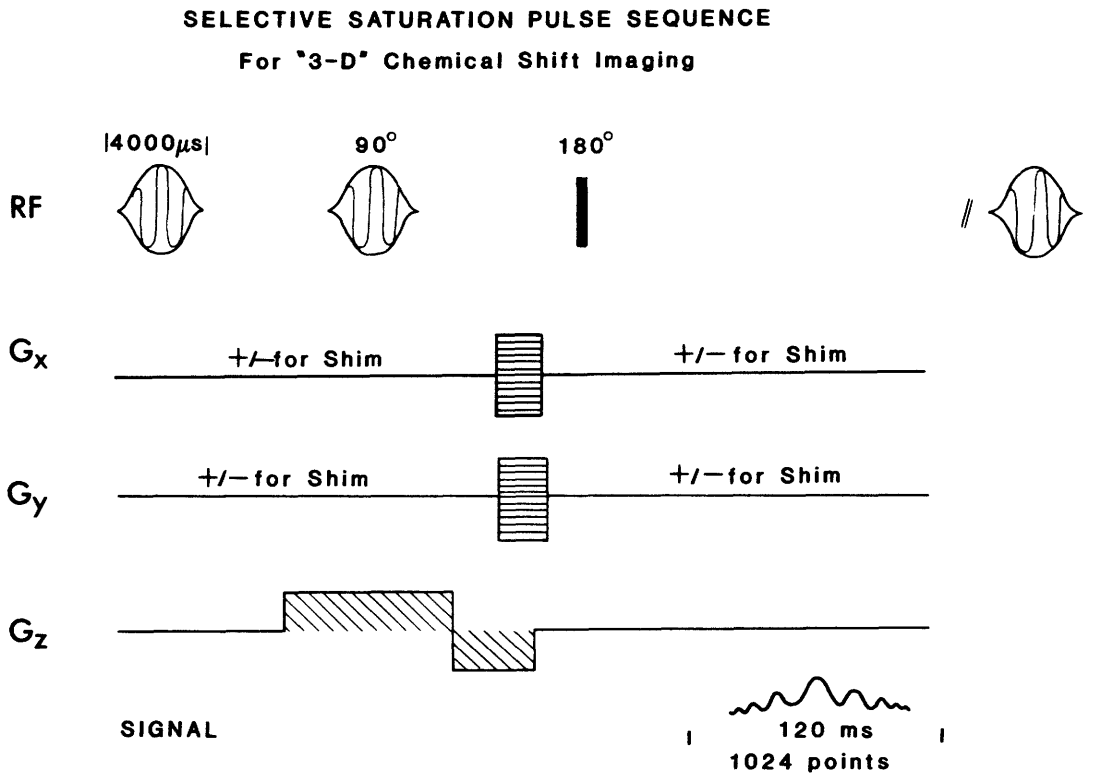

Figure 19. Pulse sequence used for selective saturation chemical shift imaging experiments. Both saturating and plane selection pulses are gaussian in profile. TR is variable, and TE fixed at 136 msec. Slight gradients G_x and G_y are used to perform B_o shimming for first order variations. Total data acquisition time was just over 120 msec.

peak lying 3.5 ppm away. This requirement (2 ppm homogeneity over an entire object) is more stringent than that required for the previous chemical shift studies (1 ppm over a voxel).

Selective Saturation: Results in Phantoms

The effect of the saturating pulse is demonstrated in Figure 20a-d. Presented are four chemical shift spectra acquired by Fourier transformation of the spin echo signal generated using the pulse sequence of Figure 19. These spectra can be generated and displayed prior to performing an imaging experiment. Two echos are averaged, and the pulse repetition time, TR, is set to 1 second. The sample consisted of a single 2 cm diameter tube filled with a 6 M aqueous lactate solution. Note that, with phase encoding gradients off, the chemical shift spectra of this high concentration lactate and water phantom clearly demonstrate the two distinct chemical moieties (a,d). By changing the frequency of the saturating pulse to correspond with one or the other spectral peak, it is possible to remove either the water or the lactate peak from the acquired spectrum (b,c). When set at the water resonance (b), greater than 95% of the signal from water protons is eliminated (saturated). Similar results are obtained from actual imaging experiments on the more dilute lactate phantoms.

The results of these imaging experiments showed that with

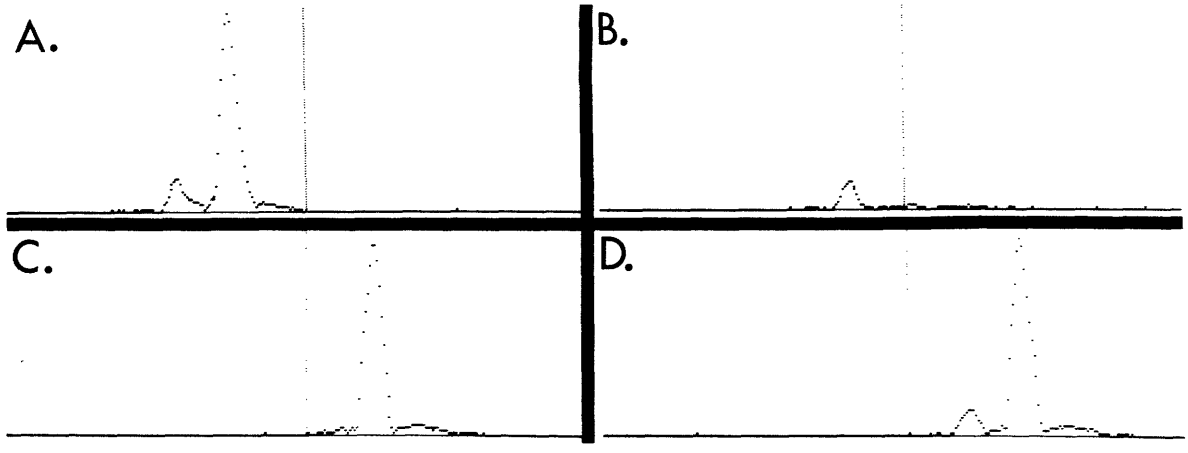

Figure 20. Frequency profiles (chemical shift spectra) from a 6 M aqueous lactate sample. Pulse sequence of Figure 19 is used, with phase encoding gradients off. Panels (a) and (d) show the entire spectrum (H_2O peak to the right of the smaller lactate peak), since the saturating pulse frequency (center line) is well offset (high and low) from either peak. By adjusting the saturating frequency to coincide with either the water resonance frequency (b) or the lactate frequency (c), these lines can separately be removed from the resulting spectra.

serial lactate dilutions down to and including 40 mM, a clear lactate image was visible when the water signal was suppressed (see Figure 21a). Without suppression, the lactate signal was not clearly visualized at or below 80 mM (Figure 21b). These results point to the potential of imaging physiologic metabolites with proton NMR.

Selective Saturation in Conventional NMR Imaging

The selective saturation technique just discussed has application in conventional NMR imaging as well. The most important is enhancing contrast in NMR studies. In particular, although NMR imaging does offer a high degree of soft tissue contrast via differences in relaxation times, chemical shift information is usually neglected in conventional studies. Chemical shift contrast can be either intrinsic (e.g., tissue lipid vs. water), or can be obtained through the use of an extrinsic chemical shift contrast agent (mineral oil in the bowel is a simple example). In order to increase the overall flexibility of NMR imaging, solvent suppression techniques can be applied to bring out both intrinsic and extrinsic chemical shift contrast. Significantly, this can be done with otherwise conventional NMR imaging techniques, bypassing the need for slower (multi-axis phase encoded) chemical shift techniques in some circumstances.

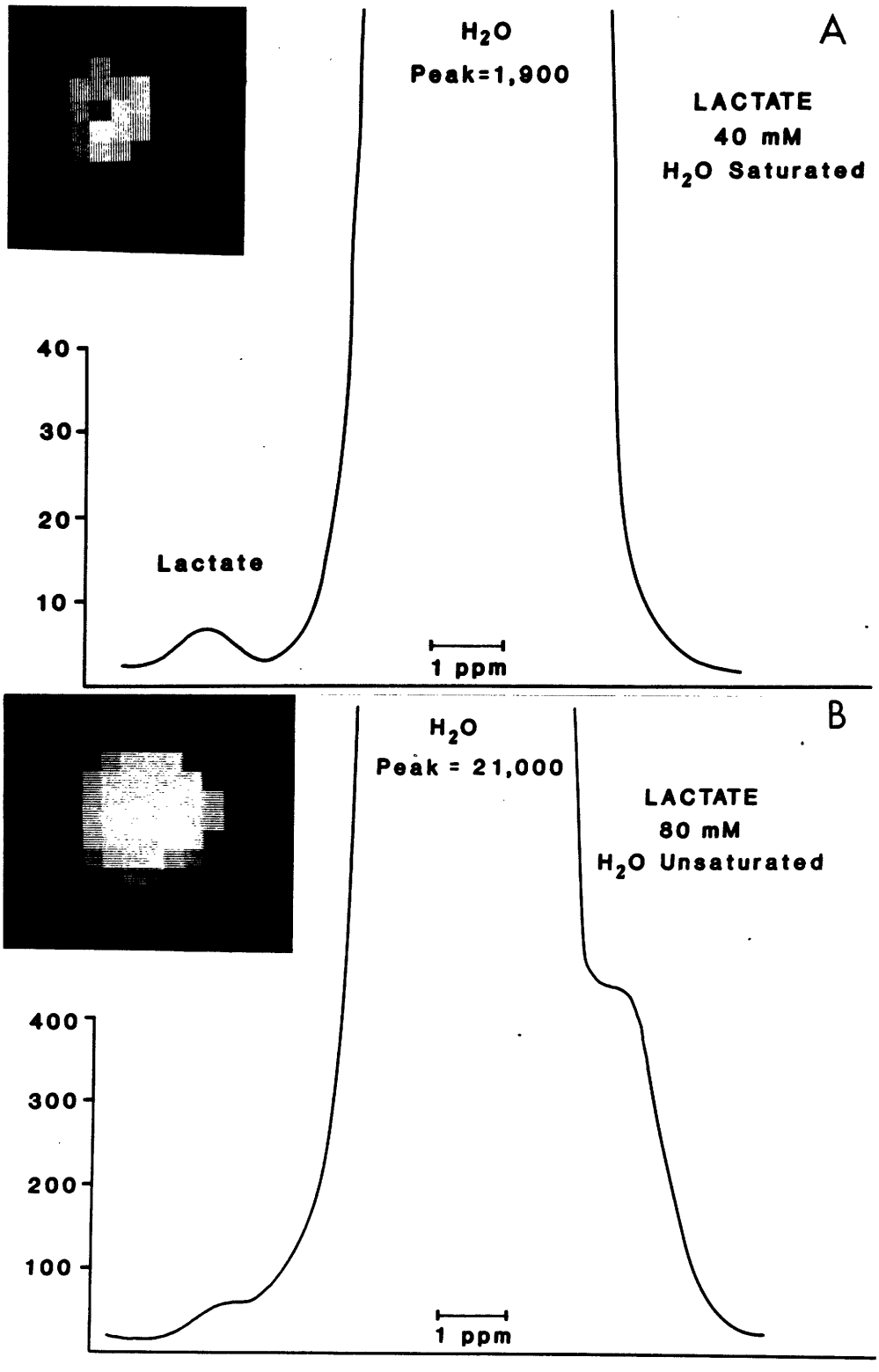

Figure 21. Total proton (lactate + water) images and chemical shift spectra extracted from a 2 x 2 pixel region centered within 2 cm diameter aqueous lactate phantoms. Panel (a) shows the results from 40 mM lactate with water suppression. Note a clear lactate peak to the left of the central water remnant. Panel (b) reports the results obtained from 80 mM lactate, this time without water suppression. Note the relative water signal is increased >10x, and no clear lactate signal is visible.

Selective Saturation 2-D Imaging: Methods and Results

Using the 1.44 tesla small bore system, selective saturation techniques were applied in conjunction with two-dimensional spin echo single slice NMR imaging. In this image protocol, the frequency selective (saturating) pulse is applied just before performing a conventional 2-D imaging experiment. As before, saturation is via a 90^{o} narrow band width pulse applied in the absence of field gradients. The TE time for this sequence is 30 msec, with 512 points acquired with a sampling interval of 30 μsec. The x-axis of this scan is frequency encoded, while the y axis spatial information is derived from phase encoding. (See Appendix for more details on conventional spin echo pulse sequences.) Figure 22 schematically represents the pulse sequence used.

The use of selective saturation to enhance intrinsic chemical shift contrast was tested on a simple in-vivo model, the human forearm. Previous chemical shift studies have demonstrated the presence of two chemical moieties in high abundance: lipid and water, within cross sections through the forearm (Figure 9). By selectively saturating out the signal from one group or the other, it becomes possible to produce an image which reflects only lipid or only water proton distribution. Relaxation weighting within this distribution is unaffected. The results are demonstrated in Figure

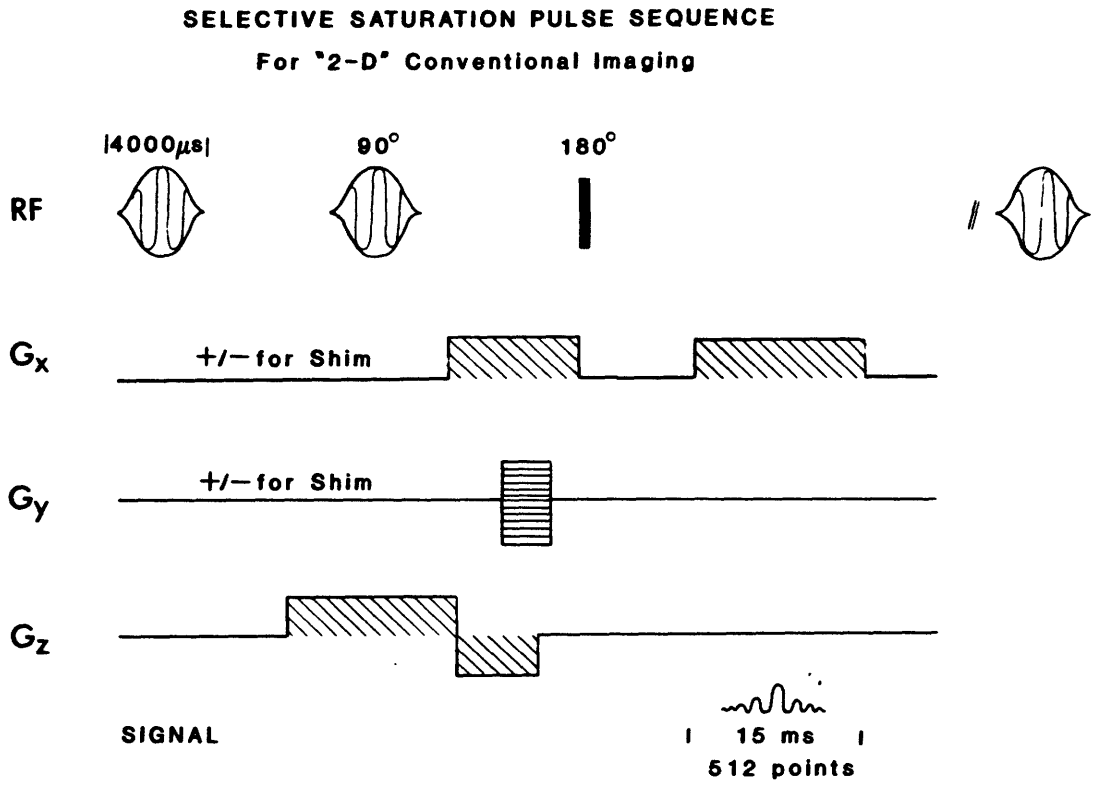

Figure 22. Pulse sequence used for selective saturation in conjunction with conventional 2D-FT imaging. TR can be varied, and TE is held fixed at 30 msec. Note the x axis is now frequency encoded, while the y axis is phase encoded. Total data acquisition time is just over 15 msec.

23a,b,c. The pulse repetition rate TR was set to 750 msec, and image time with two signal averages was 3 minutes. 128 phase encoded steps were applied along y, leading to spatial resolution of <1 mm. With image times no greater than conventional NMR methods, the chemical shift contrast within diverse tissues is thus easily demonstrated.

Discussion

Two distinct applications of a single NMR technique, selective saturation, have been introduced. In using this technique to visualize dilute chemical moieties such as lactate, proton NMR imaging will take the significant step towards providing physiologic as well as anatomic information. The role of lactate in the etiology of irreversible CNS damage during ischemic insult makes imaging of this metabolite particularly important (16,83). The association between lactate concentrations approaching 25 mM and both a decrease in high energy phosphates (84) and cerebral edema and necrosis (85) emphasizes the clinical impact anatomic mapping of this compound may have. Lactate levels are also known to be significantly elevated in other ischemic tissues, in particular ischemic myocardium (40). Although other nuclei, such as phosphorus (^{31}P), can provide similar information on cellular energy metabolism, the ability to utilize proton NMR with water suppression offers

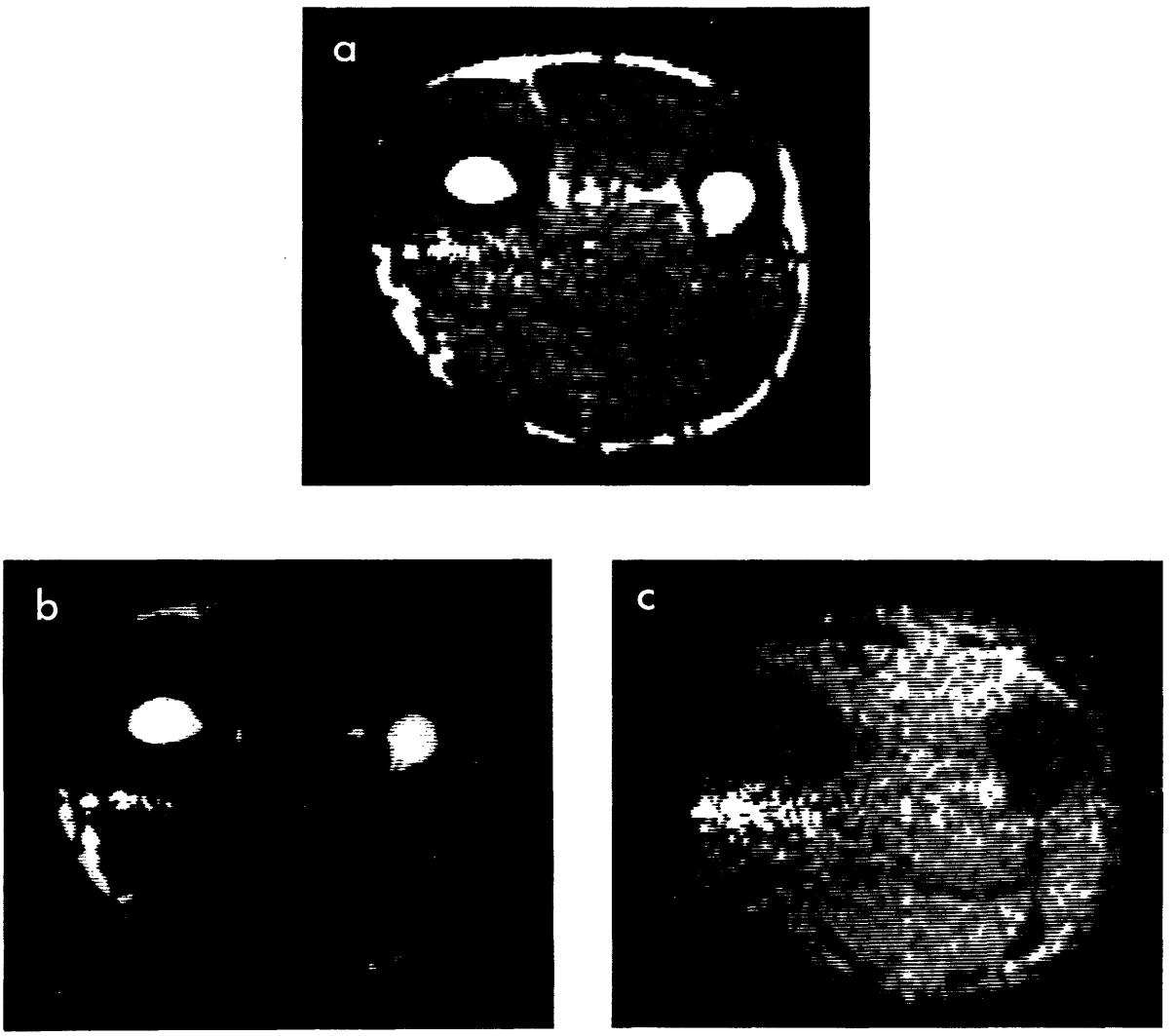

Figure 23. Three views through a normal human forearm using the sequence shown in Figure 4. Panel (a) shows the total proton image, with the saturating pulse offset. Panels (b) and (c) show lipid and water images respectively, with the saturating frequency set for water resulting in a "lipid" image in (b), and for lipids resulting in a "H_2O" image in (c). The presence of some signal from subcutaneous fat within the water image and fall-off in water signal intensity is due to inhomogeneity in B_o over the relatively large area encompassed by this image. Image time for each view was 3 minutes.

distinct advantages, including the intrinsic greater sensitivity of the hydrogen versus phosphorus nuclei (>6x for constant B_o) and more favorable relaxation times; the protons in lactate, for example, have a longer T_2 and shorter T_1 than high energy P-31 nuclei, allowing for more efficient collection of imaging data. The ability to acquire and average multiple spin echoes will also improve sensitivity. Imaging times can thus be substantially less with better spatial resolution, ultimately making these examinations practical with field strengths of 1.5 tesla and above. From this initial experience with lactate, a goal of <20 mM sensitivity with imaging times of 30 minutes should be attainable with the new generation of NMR imagers under construction. This should be sufficient to study in-vivo the response of both brain and muscle to ischemia and infarction.

Utilizing selective saturation with conventional imaging methods also opens new possibilities. While probably not applicable for imaging very dilute compounds such as lactate, the ability to form distinct lipid and water images with resolution and in times completely comparable to total proton images should find application in quickly evaluating the fat content of mass lesions and fatty livers. Also, the high degree of contrast afforded by using chemical shift differences can rival that found in contrast enhanced X-ray studies. This will allow for projective imaging methods to

be used (analogous to routine X-ray bowel contrast and angiogram studies), a highly efficient way to examine large areas of a convoluted structure not possible using relaxation time contrast alone. NMR will be capable of performing projection imaging in times equivalent to that needed for only a single 2-D slice (in fact, a 2-D technique without initial plane selection is exactly this). This offers the opportunity to develop NMR contrast media, for example intralumenal bowel agents, which act either as chemical shift reagents to shift the resonance frequency of water or which have intrinsic chemical peaks offset from those of surrounding tissue. These are currently being explored at the MGH.

These opportunities have a cost. Most important (and costly) is the need for magnetic field homogeneity, where about 2 ppm over the whole imaged region will be necessary. This is certainly greater than most imagers currently in use. Newly designed machines with spectroscopic capabilities should meet this requirement. Effects of magnetic susceptibility variation do not appear in general prohibitive, at least for studies of the head (see Chapter V). A number of pitfalls also exist. In efforts to image lactate, an important consideration will be the presence of free lipid, with its dominant chemical shift frequency closely juxtaposed to the terminal CH_3 of lactate. At least

in the brain, however, the lack of significant mobile lipid should lessen this concern (15). Signal influx by regions of surrounding subcutaneous fat can also be lessened, by applying selective excitation schemes used routinely today to perform magnification or "zoom" imaging. While fat and water imaging produce no new obstacle besides B_o homogeneity, efforts to make wider use of chemical shift contrast depend on the ability to develop safe and effective contrast agents. The use of agents with high lipid content, such as mineral oil, may find some important applications. Contrast media with chemical shifts distinct from either lipid or water will be more generally useful, because of the large amount of lipid (fat) present in and around many normal tissues.

Despite these obstacles, it seems likely that the tools of the NMR spectroscopist will become increasingly important for the imager as well. The application of basic physical principles, so characteristic of advances in magnetic resonance imaging to date, should continue to expand NMR's role within the imaging community.

VIII. Concluding Remarks

The Dissemination of PCSI Techniques

The work presented in this thesis displays the potential of performing chemical shift imaging using proton NMR, and as such is a feasibility study. The results are quite promising. Phantom data acquired using field strengths in current clinical use (1.5 tesla) have shown PCSI capable of spatial resolution of a few millimeters, and 1 ppm spectral resolution, in reasonable imaging times. In-vivo models have shown the ability to resolve fat from water protons in diverse tissues, and to quantitatively measure fatty infiltration in the liver. Furthermore, PCSI and the application of the spectroscopic technique of solvent suppression have allowed 40 mM lactate solutions to be imaged, and offers the potential of performing a wide range of studies utilizing chemical shift contrast.

Feasibility is however a different matter from utility, and in a clinical setting new imaging modalities must compete with more established techniques by providing information more accurately, cheaply, easily, or with greater safety. These constraints on the dissemination of new technology are about to become even more rigorous as prospective payment and diagnostic related groups (DRG's) reshape the radiologic landscape. In this fast approaching era additional imaging

studies will be financial burdens to hospitals rather than revenue resources. Incremental amounts of new information gained will need to be justified by their impact on clinical management and ultimately by their net effect on hospital productivity. Of course PCSI is not alone in having to account for its effectiveness, and NMR imaging in general will soon find itself answering similar questions. While research institutions and teaching hospitals may for a while have the luxury of performing both CT and NMR scans for example, the results of both studies will be scrutinized to determine which one is best in what situations. Considerable cost pressures will be brought to bear, forcing a decision on which test should be ordered. The decision to perform the relatively slow and hence costly PCSI exam will be even more closely studied.

Factors other than cost will also help determine whether PCSI enjoys widespread use in the future. As is well known, policy shapes technology as often as the other way around (86). In NMR this means that corporate and hospital boardrooms and the federal and state governments will significantly influence what kind of NMR machines are made, how capable they are, and where and when they are purchased. A relevant case is the decision by General Electric to design and sell 1.5 tesla imagers. This decision was dictated at least in part by their desire to influence the NMR buying

market by touting the advantages of high field strengths not yet available. In so doing they may well have set the trend all other manufacturers will follow. The result is that high field strength imagers, nicely capable of PCSI, should be available in large numbers. This is true despite the fact that the optimum field strength for most NMR proton imaging studies is not yet known, and may in fact lie well below 1.5 tesla (87).

The Clinical Role of PCSI

With this backdrop, the task of predicting the clinical role for PCSI is not easy. At present only feasibility can realistically be evaluated, and the studies in this thesis can provide only a starting point for determining what could be clinically important in the future. For example, fatty liver disease in humans should be amenable to PCSI evaluation, however uncertainty remains in the selection of appropriate patients. For many patients xenon scans will be sufficient and for others liver biopsy will be dictated for other reasons, avoiding the necessity of non-invasive study. However, in small children with diseases such as Reye's syndrome and in pregnant females, the advantages of PCSI may outweigh the costs.

Evaluation of various neuromuscular disorders should be possible using PCSI, and may provide another case where

benefits outweigh costs. Several disorders, in particular the muscular dystrophies, motor neuron diseases, polymyositis (and other collagen-vascular myopathies), and alcoholic, corticosteroid (88), and lipid storage myopathies (89) show various patterns of abnormal lipid accumulation (90). Although lipid in the form of droplets does occur in normal muscle fibers [more so in Type I than in Type II fibers of Dubowitz and Pearse (91)], it accumulates significantly in degenerating muscle fibers (92,93).

The diagnostic, clinical course and response to therapy of these diseases require careful and periodic clinical and muscle tissue evaluation, the latter requiring serial muscle biopsies. With PCSI, a volumetric quantitative measure of lipid buildup could be obtained non-invasively to monitor the clinical state, and could be correlated with the histologic and chemical analysis of a muscle biopsy. Again the lack of risk associated with NMR studies may make this technique particularly suitable for children, pregnant and debilitated patients, and eventually in-utero studies. Initial studies of this kind are currently being designed at the MGH.

A third area on which PCSI may have impact is in the evaluation of unknown mass lesions. For example in studying the brain, lipid content in lipomas and developmental tumors (epidermoid, dermoid, teratomas) could be more precisely evaluated directly with PCSI in these fatty lesions.

However, CT is in general good at characterizing fatty masses on the basis of decreased X-ray attenuation, and it is in such applications as these that the incremental benefit of quantitatively knowing fat content may not justify the expense and inconvenience of an additional study. However, this should not preclude the initial evaluation of PCSI for this or other applications, since cost/benefit ratios can only be determined when the benefits as well as costs are well understood. For example, if tumor grade were correlated with lipid content (as may be true in necrotic lesions) in such a way as to preclude biopsy evaluation, benefits would outweigh costs.

In the realm of proton chemical shift imaging, application of solvent suppression techniques to allow imaging of metabolites such as lactate in the brain or myocardium is both most speculative and most exciting. Because very high field strength (> 2 tesla) will probably be needed to perform lactate imaging in reasonable times, and large imagers of this kind have not yet been built, access to lactate imaging capabilities will be governed by all the political and marketing influences discussed earlier, as well as by technical limitations. In this case the situation is very analogous to positron emission tomography (PET) scanning, which is in fact a competing technology in that both measure physiology directly. In the case of PET, the

high initial and carrying costs, as well as the limited patient population that could benefit from the exam as the technology currently exists, have conspired to severely limit its dissemination. The same will likely be true of lactate or other NMR metabolite imaging, at least in the early stages. One factor which may modify this is the advancement of therapeutic regimens which would benefit from precisely distinguishing infarcted from ischemic tissue, for example emergency coronary angioplasty. Without a therapeutic endpoint such metabolic studies become meaningless, but gain greatly in importance as the potential therapeutic benefits grow. For this reason a technique initially of only research value can become with time a clinical necessity. Certainly a reasonable goal for now should be the refinement of techniques to allow this study to be performed in-vivo and again this is currently being investigated at the MGH.

The use of solvent suppression to perform high contrast 2-D and projective imaging studies is also at this point speculative. This is in part because appropriate non-toxic contrast agents have not yet been identified. The most important limitation of this technique is the excellence of the competing X-ray technology, which offers high quality and speed, ready availability, low cost, and a long record of safety to the patient. As before, the one area where the PCSI technique may have clinical utility is in examining

patients at risk to radiation exposure, the pregnant and small children. These groups alone could not justify the cost of a unit dedicated to this purpose, however machines capable of performing this study may on occasion be called upon to do so.

Other Nuclei

Finally, a few comments are appropriate on the application of chemical shift imaging techniques to studying other nuclei. The list of biologically important nuclei should include P-31, C-13, F-19 and Na-23. Of these, crude chemical shift images of natural P-31 in normal and ischemic cat heads, and normal human leg muscle, have been performed (30), and pilot studies in our own laboratory have been performed using F-19 containing anesthetic agents and blood analogues. No in-vivo imaging studies of C-13 have yet been made, but the ability to monitor pharmacological or metabolic agents labeled with a high abundance of C-13 makes this nucleus attractive in some respects. Na-23 imaging has been performed in humans (29), and perhaps the use of extracellular shift reagents may lead to the use of chemical shift imaging techniques.

The major problem inherent in the study of these nuclei is a lack of sensitivity. Except for F-19, at constant B_o the intrinsic NMR sensitivity of the other nuclei is many

times less than that of protons. In addition, in performing natural abundance studies, the low concentrations (150 mM for Na-23, <20 mM for P-31) of these nuclei in-vivo lead to diminished S/N, requiring lengthy studies at low resolution. For these reasons, P-31 imaging studies may be supplanted with proton metabolite studies, which also have low abundance but have intrinsic sensitivity and relaxation advantages over P-31. C-13 is likely to be even less amenable to realistic imaging studies, especially given the expense of concentrated C-13. Both P-31 and C-13 may well be investigated using surface coil technology. The limitation here will be obtaining adequate spatial localization, a significant problem with its own potential set of solutions (94).

F-19 has some advantages over these other nuclei. With a relatively high intrinsic sensitivity and practically zero natural abundance, studies using pharmacologic agents containing F-19 may be practical. One such study designed at the MGH includes investigating the biodistribution of multiple agents concurrently available (lipophilic general anesthetic agents and intravascular synthetic blood analogs), using differences in the chemical shifts of the attached fluorine as specific drug markers. One goal of this work would be to develop a marker of tissue blood perfusion. Again sensitivity is likely to be the most significant technological problem, since very high concentrations of most

of these drugs are toxic. The design of new agents, multiply fluorinated to boost sensitivity while maintaining non-toxic concentrations, is certainly a possibility.

Conclusion

At this time no clear role exists for spectroscopic imaging techniques in clinical practice. Nevertheless chemical shift imaging today is at least as well developed as all of NMR imaging was but five years ago. The dramatic advances in conventional imaging techniques witnessed recently offer the hope that spectroscopic data within an imaging context will significantly contribute to future health care.

Appendix - Spin Lattice Relaxation Time Measurements in Planar NMR Imaging: Corrections for Plane Selection and Pulse Sequence

Introduction

Proton (^1H) NMR imaging can provide both high quality structural information and some degree of in-vivo tissue characterization using T_1 (spin-lattice) and T_2 (spin-spin) relaxation times. These parameters may provide diagnostic specificity and/or the ability to monitor various medical therapies. To facilitate these goals it is necessary to obtain accurate and reproducible quantitative measurements, allowing NMR image data comparisons from one machine over time and between different NMR systems operating at the same frequency. Methods using combination pulse sequences, which acquire two data points per pulse repetition cycle, have been developed to measure T_1 in three-dimensional (volumetric) (95) and two-dimensional (planar) imaging schemes (96). These techniques employ magnetization inversion to generate T_1 weighting, and thus are modifications of traditional inversion recovery techniques (97). It has been known for some time that measurements made using progressive saturation or saturation recovery pulse sequences are an efficient means to collect T_1 data (98,99) and thus have also been applied within an imaging context (100). However, the details of an

imaging experiment, which differ in significant ways from simpler spectroscopic techniques, will alter the analysis used to calculate relaxation times. In particular, the use of spin echoes (1Ø1) to acquire data in imaging, and methods of selective excitation used for plane selection in 2-D studies (and 3-D chemical shift studies), can modify the behavior of the spin system in such a way that significant errors will be introduced in calculating relaxation times if traditional analysis is used. The purpose of this appendix is first to calculate the values for signal intensity expected from a saturation recovery (SR) type image formed using spin echoes and 2-D selective excitation (38), second to determine the error introduced in measurement of T_1 relaxation times by failing to account for imaging details (and hence allow correction for this bias), and third to present the results of phantom studies corroborating the validity of the above analysis.

Imaging Pulse and Gradient Sequence

An illustration of the RF pulses and magnetic field gradients used in spin echo planar imaging is presented in Figure 24. Two features distinguish this sequence from the traditional 90^{o}-TR-90^{o} SR pulse pattern. First, data are not recovered from the FID following each 90^{o} pulse, rather data are acquired from a spin echo produced by a 180^{o} refocusing

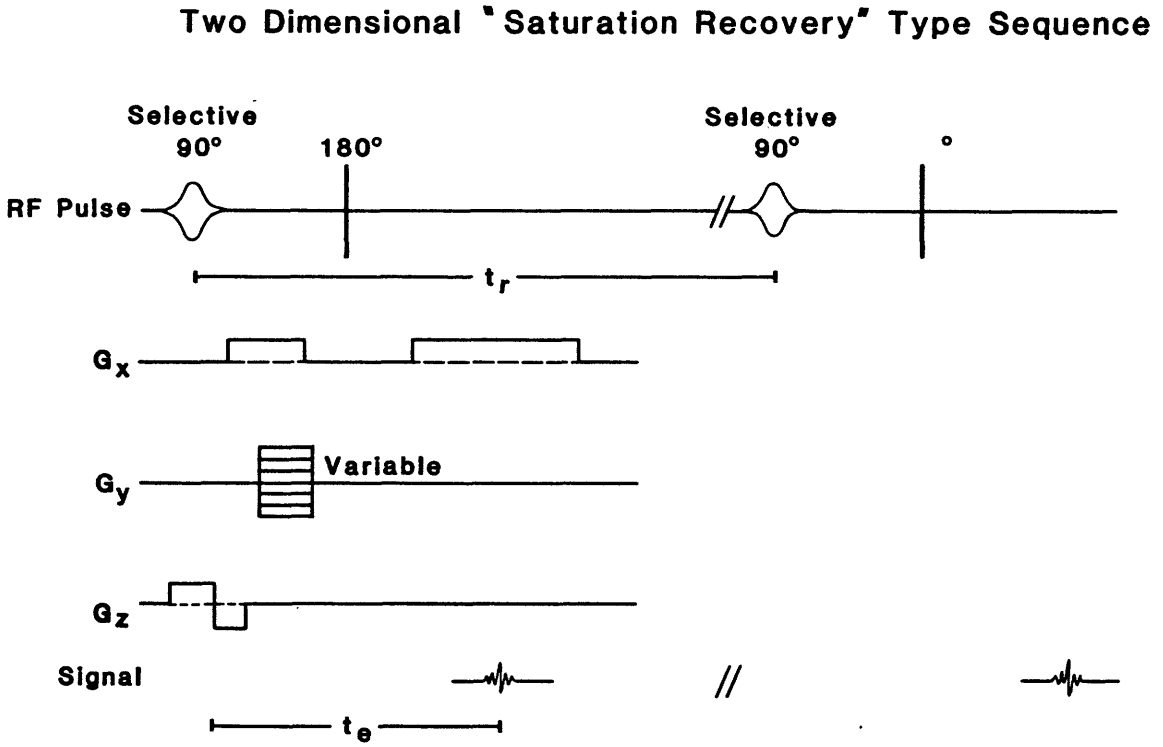

Figure 24. Schematic representation of the "saturation recovery" pulse sequence used for two-dimensional imaging and calculations of T_1 relaxation times. The selective pulse is gaussian in amplitude profile, and TE is fixed at 32 msec. The 90^{o}-90^{o} interval, TR, is varied from 200 to 2000 msec.

pulse, applied 16 msec after each 90° pulse. Second, plane selection in this imaging scheme is achieved using a gaussian selective excitation pulse, which excites only those spins whose resonance frequency, defined by application of a magnetic field gradient perpendicular to the desired imaging plane, lies within those frequencies encompassed by the Fourier Transform of the gaussian RF envelope (102,103). The effect, as discussed below, is that most spins will undergo less than a 90° nutation within the actual excited volume. In acquiring data for this thesis the plane selection process is performed only for the initial saturating 90° pulse; the 180° refocusing pulse will produce no transverse magnetization in regions initially unexcited and hence can be of broad bandwidth in single slice imaging techniques.

In-plane spatial localization for 2-D conventional imaging is performed using a 2-dimensional Fourier Transform technique (55) whereby one dimension is encoded by application of a constant gradient during echo acquisition, and the orthogonal direction is encoded by sequential phase encoding gradients. For simplicity all images for this study were acquired using this technique, since T_1 measurements will be independent of the in-plane encoding scheme. The results are equally applicable to chemical shift methods, where both x and y axis spatial encoding is performed with phase encoding. Images using the above pulse sequence can be

acquired at various 90^{o}-90^{o} intervals, TR. The 90^{o}-180^{o} interval was held fixed for this study at 16 msec.

Mathematical Model

In a general sense, for any sufficiently small volume of spins, the pulse sequence above will act as an -180^{o} sequence, where the α^{o} read pulse will take on a value dependent on both the position of the spins within the volume of the selected slice and the overall pulse amplitude. For this sequence, the equilibrium solution to the Bloch equations for $\alpha \leq 180^{o}$ can be derived as follows. Let $M_n(\alpha)$ be the longitudinal component of magnetization immediately preceding the n^{th} α^{o} pulse, $M_n(180)$ the longitudinal component preceding the n^{th} 180^{o} refocusing pulse, and $M_{n+1}(\alpha)$ and $M_{n+1}(180)$ the values of longitudinal magnetization which precede the respective subsequent pulses. The solution for $M_n(180)$ in terms of $M_n(\alpha)$ can be immediately written from the Bloch equation for longitudinal magnetization (34):

$$M_n(180) = M_o(1-e^{-\frac{1}{2}TE/T_1}) + M_n(\alpha) \cdot \cos\alpha \cdot e^{-\frac{1}{2}TE/T_1} \quad (1)$$

where M_o is the longitudinal equilibrium magnetization, T_1 is the longitudinal relaxation time of the spin system, and 1/2TE is the time interval between the α^{o} and 180^{o} pulses.

(TE is defined as the time from the 90° pulse to the peak of the echo.) The solution for $M_{n+1}(\alpha)$ in terms of its preceding value $M_n(180)$ can be written similarly:

$$M_{n+1}(\alpha) = M_o(1-e^{-(TR-\frac{1}{2}TE)/T_1}) - M_n(180)e^{-(TR-\frac{1}{2}TE)/T_1} \quad (2)$$

where TR is defined as the time between α pulses, and thus the term (TR - 1/2TE) is the 180°- α^o pulse interval (see Figure 24). Substituting equation 1 into equation 2 and rearranging gives:

$$M_{n+1}(\alpha) = M_o(1-e^{-(TR-\frac{1}{2}TE)/T_1} + e^{-TR/T_1}) - M_n(\alpha) \cdot \cos\alpha \cdot e^{-TR/T_1} \quad (3)$$

However, after sufficient pulses a steady state will be established for which:

$$M_{n+1}(\alpha) = M_n(\alpha) \quad (4)$$

and thus one can solve equation 4 for $M_n(\alpha)$ using equation 3 to obtain:

$$M_n(\alpha) = M_{n+1}(\alpha) = \frac{M_o(1-2e^{-(TR-\frac{1}{2}TE)/T_1} + e^{-TR/T_1})}{(1 + \cos\alpha \; e^{-TR/T_1})} \quad (5)$$

By acquiring spin echo data at time TE after the α^{o} pulse, the actual signal detected can be written:

$$S \propto e^{-TE/T_2} \cdot \sin\alpha \cdot \frac{M_o(1-2e^{-(TR-\frac{1}{2}TE)/T_1} + e^{-TR/T_1})}{(1 + \cos\alpha\ e^{-TR/T_1})} \quad (6)$$

where T_2 is the transverse relaxation time of the spin system. One observation is worth noting at this point. The effect of acquiring spin echo data via application of a 180^{o} pulse is not restricted to the T_2 effect; the addition of a 180^{o} refocusing pulse disturbs the longitudinal magnetization as well. Even when $\alpha = 90^{o}$, equation 6 still contains terms with (TR - 1/2TE). Only in the limiting case where TR >> TE and $\alpha = 90^{o}$ does equation 6 reduce to:

$$S \propto e^{-TE/T_2} M_o(1-e^{-TR/T_1}) \quad (7)$$

This expression, which contains the familiar $(1-e^{-TR/T_1})$ SR term, is used by some centers as a basis for T_1 measurement (100).

The effect of a plane selection pulse will depend on the profile of the excited slice. For these data, and in all chemical shift studies in this thesis, a gaussian RF pulse envelope is used. To a good approximation, the distribution of pulse angles will therefore also have a gaussian profile

when the pulse is applied in the presence of a linear gradient (54). If the pulse amplitude is such that centrally located spins will be rotated through a full 90^{o}, protons on either side will have pulse angles less than 90^{o}, depending on their distance from the center. In order to properly estimate signal intensity as a function of T_1 and TR it is necessary to integrate equation 6 over the distribution of pulse angles α. For a gaussian pulse one can write:

$$\alpha = \alpha_o e^{-z^2} \tag{8}$$

where α_o is the maximum (central) pulse angle in degrees, and z a length along the axis perpendicular to the excited slice. Substituting this expression into equation 6, and integrating over all z, the expression for signal intensity S, as a function of TE, TR, T_1 and T_2, will take the form:

$$S \propto M_o e^{-TE/T_2} (1-2e^{-(TR-\frac{1}{2}TE)/T_1} + e^{-TR/T_1}) \int \frac{\sin(\alpha_o e^{-z^2})\,dz}{1 + \cos(\alpha_o e^{-z^2}) e^{-TR/T1}} \tag{9}$$

This model assumes phase coherence of magnetization over the pulse distribution and cylindrical symmetry over the effective slice thickness and is thus independent of slice thickness (54). In principle the method can be applied to non-gaussian distributions, and in particular can be applied

to correct for distributions designed to approximate more closely rectangular slice excitation, by integration over the appropriate profile.

Experimental Methods and Results

In order to test the validity of these equations in practice, and to judge the magnitude of their effect on actual relaxation time measurements, two experiments were performed. The first of these involved mathematically modeling the behavior of the spin system using the equations derived above. Numerical integration of equation 9 was performed for 9 values of T_1 ranging from 100 to 900 msec, and for 6 values of TR (192, 292, 492, 892, 1292, 2058 msec) corresponding to those acquired using patient imaging protocols (38). TE was fixed at 32 msec, and α_o set equal to 90^o, approximating actual imaging settings for 2-D conventional studies. Thus for each value of T_1 and TR (54 in all) equation 9 was evaluated to provide information on relative signal intensity expected from an imaging experiment which used the pulse sequence shown in Figure 24. The values for signal intensity at the six values for each T_1 evaluated were then fit to the traditional equation for SR data:

$$S = M_o(1-e^{-TR/T_1}) \qquad (10)$$

For each of the 9 true values of T_1 tested, the resulting T_1 fit to equation 10 was compared to the actual T_1 value input into equation 9, an effort to determine the errors in using the traditional equation as the basis for T_1 measurement.

The results of this analysis are shown in Table I. Note that the fitted values for T_1 were consistently higher than the actual T_1 values; an increase approaching 70% is evident for long T_1. While the values calculated in Table I depend on both the TR values chosen and TE, T_1 is over-estimated regardless of TR and TE. This analysis was repeated for the TR and TE values used in the chemical shift experiments of Chapter VI. The results are shown in Table II.

The second experiment was designed to determine if the mathematical model accurately reflected the true imaging experiment. T_1 values were obtained independently on six phantoms at various concentrations of $CuSO_4$ and $MnCl_2$ using the standard 180^o-TI-90 inversion-recovery sequence. Data were obtained using a .15 tesla prototype resistive magnet NMR imaging system (Technicare Corporation), operating in the "spectrometer" mode, i.e., without magnetic field gradients applied (95). Using the SR sequence of Figure 24, NMR images of each phantom were acquired at six TR values (192 - 2058 msec) using the same imaging system. Resulting signal intensity measurements were fit as above to equation 10 where, again, comparison between actual T_1 values

and those generated using the traditional SR equation could be made. In addition, T_1 values from these image data could be compared to values generated by computer integration shown in Table I, thus testing the validity of equation 9 in actual imaging experiments.

The results from these measurements are shown in Table III and plotted, along with those of Table I, in Figure 25. Note in Table III that, as expected, values of T_1 calculated by fitting the traditional SR equation to image data were in error by 30% to 70%, over-estimating the actual T_1. Figure 25 shows that the measured T_1 values using the above curve fitting were in close agreement with those generated by computer modeling of regions with similar T_1's. This is the anticipated result if equation 9 accurately reflects the behavior of the spin system in an imaging context.

Discussion

The assessment of T_1 and T_2 relaxation time values using standard NMR spectroscopy has provided a method to characterize various disease processes (see Chapter II). These same NMR parameters are responsible for the excellent soft tissue contrast exhibited in conventional NMR images. It is hoped that these parameters might provide a useful degree of *in-vivo* tissue characterization, thus allowing for

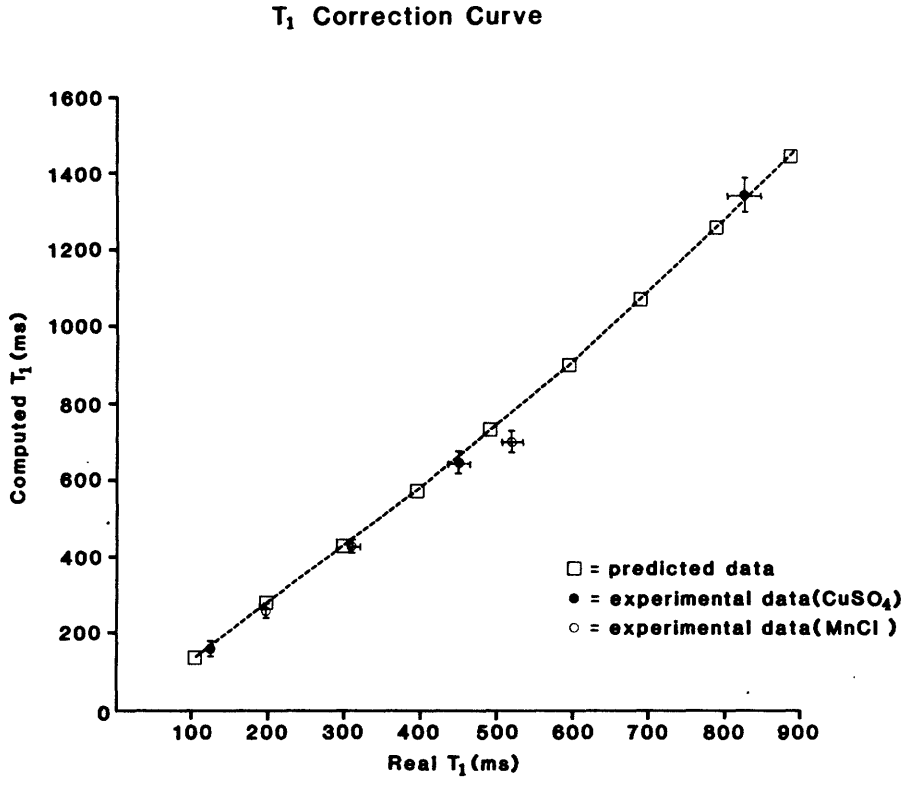

Figure 25. Predicted computer model and experimental data of the relation between T_1 fit using the conventional SR equation (computed T_1) and the actual T_1 value (real T_1). Both data sets show that significant errors in T_1 will be made in using the simple $(1 - e^{-TR/T1})$ relation for T_1 determination.

diagnostic specificity, staging of various disease processes, and monitoring of various medical and surgical therapies in both conventional and chemical shift imaging contexts. To facilitate both the development and clinical evaluation of any or all of these aims, the relaxation time values obtained using NMR imaging techniques must be reproducible and as accurate as possible.

Determination of relaxation times in biological systems is inherently problematic. In <u>in-vitro</u>, non-imaging experiments, multicomponent relaxation behavior has been observed, making single value estimates of T_1 or T_2 somewhat arbitrary (104,105). In an <u>in-vivo</u> imaging context, flow, motion, diffusion, partial volume artifacts, and both the temperature and frequency dependence of relaxation times can all influence T_1 and T_2 measurement. Notwithstanding, parameter quantification in NMR imaging may be clinically important for the reasons noted above; however, care in interpretation must clearly be exercised. The above experiments demonstrate that the details of the pulse sequence and spatial encoding methods must be accounted for if accurate relaxation time determinations are sought. This study shows that utilization of selective irradiation and 180^{o} refocusing pulses for spin echo acquisition will significantly modify the results expected from a traditional saturation recovery type protocol designed to measure T_1.

The concordance in the values of actual versus computer generated data suggests the feasibility of using a mathematical model to correct for system-related influences of the kinds discussed above. In particular, Figure 25 can be used in conjunction with simple curve fitting techniques to calculate corrected values for T_1, avoiding the more difficult task of fitting equation 9 directly. (Note, however, that the curve presented here will be correct only for the values of TR and TE tested.) This technique will also, within the limits imposed by the assumption of cylindrical uniformity, be both frequency and slice thickness independent. In addition, since numerical techniques can be applied in carrying out the integration through the slice profile, measurements of the actual profile can be used directly when non-gaussian distributions are either intended or, due to system operating characteristics, suspected.

This latter point can be made use of in a more general sense to tackle the difficult problem of RF field inhomogeneity, which affects the uniformity of the RF pulse angle within the image plane and is manifested on many NMR images as a peripheral fall-off of signal intensity. This RF inhomogeneity can significantly affect relaxation time measurements made across the image plane. By measuring the maximum RF angle delivered point by point throughout the imaging region, an expression such as equation 9, with

additional terms for non-180^{o} refocusing pulses, can be evaluated on a regional basis, and an in-plane correction table calculated. A similar correction for RF inhomogeneity could be applied to 3-D volumetric acquisition techniques as well using an expression analogous to equation 6, since in the 3-D case broad band, non-selective pulses are used. and integration over the slice is unnecessary. In this manner a single set of measurements would suffice to correct for any intrinsic RF inhomogeneities; smaller variation brought on by differences in the coil loading by different patients would be more difficult to correct by this method.

TABLE I

Computer Modeled Data from Six Point

Fit to $M_o(1-e^{-TR/T1})$

True T_1	Computed T_1
100	133
200	277
300	422
400	573
500	732
600	900
700	1,077
800	1,264
900	1,460

TR values used = 192, 292, 492, 892, 1292, 2058 msec.

Pulse sequence as in Figure 19.

Signal intensity calculations at each TR value derived from numerical integration of equation (9).

TABLE II

Computer Modeled Data from Four Point

Fit to $M_o(1-e^{-TR/T_1})$

True T_1	Computed T_1
100	141
200	305
300	493
400	710
500	960
600	1,245

TR values used = 149, 245, 605, 965 msec

TE = 51 msec

Signal intensity calculations at each TR value derived from numerical integration of equation (9).

TABLE III

Phantom Data From Imaging Experiment Using Six Point Fit to $M_o(1-e^{-TR/T_1})$

	Concentration	Measured T_1	Computed T_1
$CuSO_4$	~ 5.0 mM	129 ± 2	164 ± 10
	~ 1.0 mM	461 ± 15	644 ± 30
	~ 0.5 mM	832 ± 25	1350 ± 40
$MnCl_2$	~ 0.3 mM	202 ± 4	263 ± 12
	~ 0.2 mM	309 ± 7	417 ± 20
	~ 0.1 mM	524 ± 15	698 ± 30

Measured T_1 calculated from an eight point IR fit, imager in "spectrometer" mode. TR and pulse sequence imaging parameters as in Table I for computed T_1.

References

1. Purcell EM, Torrey HC, Pound RV. Phys Rev, 69:37, 1946.
2. Bloch F, Hansen WW, Packard M. Phys Rev, 69:127, 1946.
3. Proctor WG, Yu FC. Phys Rev, 77:717, 1950.
4. Dickinson WC. Phys Rev, 77:736, 1950.
5. For general NMR theory, see, for example, Slichter S. Principles of Magnetic Resonance, New York: Springer-Verlag, 1980.
6. Bersohn R. Annu Rev Phys Chem, 11:369, 1960.
7. Shulman RG. Annu Rev Phys Chem, 13:325, 1962.
8. Cohn M, Nageswara Rao BD. In Pullman B, Frontiers in Physicochemical Biology, New York: Academic Press, pp 191-211, 1978.
9. Brown TR. J Comput Assist Tomogr, 5:301, 1981.
10. Cohn M, Hughes TR Jr. J Biol Chem, 235:3250-3253, 1960.
11. Hollis DP, Nunnally RL, Taylor GJ, et al. J Magnet Res, 29:319-330, 1978.
12. Bocian DF, Chan SI. Annu Rev Phys Chem, 29:307-335, 1978.
13. Jacobs RE, Oldfield E. Prog Nucl Magnet Res Spectrosc, 14:113-136, 1981.
14. Wyrwicz AM, Schofield JC, Burt CT. In Cohen JS (ed), Noninvasive Probes of Tissue Metabolism, New York: Wiley-Interscience, pp 149-171, 1982.
15. Shulman RG, Brown TR, Ugurbil K, et al. Science, 205: 160-166, 1979.
16. Behar KL, DenHollander JA, Stromski ME, et al. Proc Natl Acad Sci USA, 80:4945-4948, 1983.
17. Chance B, Nakase Y, Bond M, et al. Proc Natl Acad Sci USA, 75:4925-4929, 1978.
18. Shaw D. J Comput Assist Tomogr, 5:299-300, 1981.
19. Ackerman JJH, Grove TH, Wong GG, et al. Nature, 283: 167-170, 1980.
20. Nunnally RL, Bottomley PA. Science, 211:177-180, 1981.
21. Jaklovsky J. NMR Imaging: A Comprehensive Bibliography, Reading, MA: Addison-Wesley, 1983.
22. Gordon RE, Hanley PE, Shaw D. Prog NMR Spect, 15:1-47, 1982.
23. Bottomley PA. J Mag Res, 50:335-338, 1982.
24. Scott KN, Brooker HR, Fitzsimmons JR, et al. J Mag Res, 50:339-344, 1982.
25. Lauterbur PC. Nature, 242:190-191, 1973.
26. Damadian R. Science, 171:1151-1153, 1971.
27. Weisman ID, Bennett LH, Maxwell LR, et al. Science, 178:1288-1290, 1972.
28. Witcofski RL, Karstaedt N, Partain CL (eds).

Proceedings of an International Symposium on Nuclear Magnetic Resonance Imaging, Winston-Salem, NC: Wake Forest University Press, 1982.
29. Partain CL, James AE, Rollo FD, Price RR (eds). Nuclear Magnetic Resonance Imaging, Philadelphia: W.B. Saunders Co., 1983.
30. Hilal SK, Maudsley AA, Simon HE, et al. AJNR, 4: 245-249, 1983.
31. Maudsley AA, Hilal SK, Perman WH, et al. J Mag Res, 51:147-152, 1983.
32. Mansfield P, Morris PG. NMR Imaging in Biomedicine, New York: Academic Press, 1982.
33. Rosen BR, Brady TJ. Semin Nucl Med, 13:308-318, 1983.
34. Farrar TC, Becker ED. Pulse and Fourier Transform NMR - Introduction to Theory and Methods, New York: Academic Press, 1971.
35. Brady TJ, Buonanno FS, Pykett IL, et al. Neurology, 32:A155, 1982.
36. Doyle FH, Pennock JM, Banks LM, et al. AJR, 138: 193-200, 1982.
37. Bydder GM, Steiner RE, Young IR, et al. AJR, 139:215-236, 1982.
38. Brady TJ, Rosen BR, Pykett IL, et al. Radiology, 149: 181-187, 1983.
39. Buonanno FS, Pykett IL, Kistler JP, et al. Radiology, 143:183, 1982.
40. Williams ES, Kaplan JL, Thatcher F, et al. J Nucl Med. 21:449-453, 1980.
41. Buonanno FS, Brady TJ, Pykett IL, et al. Neurology, 32:A163, 1982.
42. Young IR, Hall AS, Pallis CA, et al. Lancet, 2:1063-1066, 1981.
43. Brady TJ, Rosen BR. In Proceedings from the National Conference on Biological Imaging. II. Clinical Aspect, in press.
44. Herfkens R, Davis P, Crooks LE, et al. Radiology, 141: 211-218, 1981.
45. Brunner P, Ernst RR. J Mag Res, 33:83-106, 1979.
46. Hinshaw WS. J Appl Phys, 47:3709-3721, 1976.
47. Meire FT, Thatcher FC. J Appl Phys, 50:4491-4502, 1979.
48. Chen C-N. J Amer Chem Soc, 97:6866-6868, 1975.
49. Bendel P, Lai C-M, Lauterbur PC. J Mag Res, 38: 343-356, 1980.
50. Cox SJ, Styles P. J Mag Res, 40:209-212, 1980.
51. Brown TR, Kincaid BM, Ugurbil K. Proc Natl Acad Sci USA, 79:3523-3526, 1982.
52. Maudsley AA, Oppelt A, Ganssen A. Forsch u Entwickl Ber Bd, 8:326-331, 1979.

53. Sutherland RJ, Hutchison JMS. J Phys E: Sci Instru, 11:79-83, 1978.
54. Kumar A, Welti D, Ernst RR. Naturwissenschaft, 62: 34, 1974.
55. Maudsley AA, Simon HE, Hilal SK. J Phys E: Sci Instru, in press.
56. Edelstein WA, Hutchison JMS, Johnson G, et al. Phys Med Biol, 25:751, 1980.
57. Lauterbur PC. Nature, 242:190-191, 1973.
58. Pykett IL. Semin Nucl Med, 13:319-328, 1983.
59. Dickinson WC. Phys Rev, 81:717-731, 1951.
60. Evans DF. J Chem Soc, 1959.
61. Orrel KG, Sik V. Annal Chem, 52:569-572, 1980.
62. Brittenham GM, Farrell DE, Harris JW, et al. New Engl J Med, 307:1671-1675, 1982.
63. Crooks LE, Mills CM, Davis PL, et al. Radiology, 144: 843-852, 1982.
64. Yoshizaki K, Seo Y, Nishikawa H. Biochim Biophys Acta, 678:283-291, 1981.
65. Gore J. In Witcofski RL, Karstaedt N, Partain CL (eds), Proceedings of an International Symposium on Nuclear Magnetic Resonance Imaging, Winston-Salem, NC: Wake Forest University Press, p 18, 1982.
66. Belton PS, Jackson RR, Packer KJ. Biochim Biophys Acta, 286:16-25, 1972.
67. Blackwood W, McMenemey WH, Meyer A, Norman RM, Russel DS (eds). Greenfield's Neuropathology, London: Edward Arnold Publishing, pp 81-ff, 1969.
68 Senftle FE, Thorpe A. Nature, 190:410-413, 1961.
69. Hoyumpa AM Jr, Greene HL, Dunn GD, et al. Digestive Diseases, 20:1142, 1975.
70. Ahmad M, Perrillo RP, Sunwoo YC, et al. J Nucl Med, 20:397, 1979.
71. Perrault J, McGill DB, Ott BJ, et al. Gastroenterology, 74:103, 1978.
72. Stark DD, Bass NM, Moss AA, et al. Radiology, 148: 743, 1983.
73. Block RE. Biochem Biophys Res Commun, 108:940, 1982.
74. Alger JR, Sillerud LO, Behar KL, et al. Science, 214: 660-662, 1981.
75. Zimmerman HJ, Maddrey WC. In Schiff L (ed), Diseases of the Liver, Philadelphia: Lippincott, p 621, 1982.
76. Alpers DH, Sabesin. In Schiff L (ed), Diseases of the Liver, Philadelphia: Lippincott, p 813, 1982.
77. Carter EA, Drummey GD, Isselbacher KJ. Science, 174: 1245, 1971.
78. Ratner AV, Carter EA, Wands JR, et al. Mag Res in Med, 1(2):164, 1984.

79. Waugh JS, Huber LM, Haeberlen U. Phys Rev, 20:180, 1968.
80. Turner DL. J Mag Res, 54:146-148, 1983.
81. Clore GM, Kimber BJ, Gronenborn AM. J Mag Res, 54:170-173, 1983.
82. Redfield AG, Kunz SD, Ralph EK. J Mag Res, 19:114, 1975.
83. Myers RE. In Fahn S, Davis JN, Rowland LP (eds), Advances in Neurology, New York: Raven Press, pp 195-213, 1979.
84. Rehncrona S, Rosen I, Siesjo BK. Acta Physiol Scand, 110:435-437, 1980.
85. Myers RE, Yamaguchi M. J Neuropathol Exp Neurol, 35: 310, 1976.
86. Mack PE. The Politics of Technological Change: A History of Landsat. Ann Arbor, MI: University Microfilms, 1984.
87. Crooks LE, Arakawa M, Hoenninger J, et al. Radiology, 151:127-133, 1984.
88. D'Agostino AN, Chiga M. Neurology, 16:257-262, 1966.
89. Bradley WG, Jenkison M, Park DC, et al. J Neurol Sci, 16:137-154, 1972.
90. Dubowitz, Brooke. Muscle Biopsy: A Modern Approach, Philadelphia: W.B. Saunders Co, 1973.
91. Prineas J, Ng RCY. Neurology, 17:1092-1098, 1967.
92. Trump BF, Ericsson JLE. In Zwerfach BW, Grant L, McCluskey RT (eds), The Inflammatory Process, New York: Academic Press, pp 35-120, 1965.
93. Reznik M, Hansen JL. Arch Path, 87:601-608, 1969.
94. Evelhoch JL, Ackerman JJH. J Mag Res, 53:52-64, 1983.
95. Pykett IL, Rosen BR, Buonanno FS, et al. Phys Med Biol, 28:723-729, 1983.
96. Redpath TW. Phys Med Biol, 27(8):1057-1065, 1982.
97. Vold RL, Waugh JS, Klein MP, et al. J Chem Phys, 48:3831, 1968.
98. Freeman R, Hill HDW. J Chem Phys, 54:3367-3377, 1971.
99. Edelstein WA, Bottomley PA, Hart HR, et al. J Comput Assist Tomogr, 7(3):391-401, 1983.
100. Crooks L, Arakawa M, Hoenninger J, et al. Radiology, 143:169-174, 1982.
101. Hahn EL. Phys Rev, 80:580-594, 1950.
102. Lauterbur PC, Dulcey CS, Lai CM, et al. In Proceedings of the 18th Ampere Congress, Nottingham, pp 27-29, 1974.
103. Mansfield P, Maudsley AA, Baines T. J Phys, E9:271-278, 1976.
104. Pearson RT, Duff ID, Derbyshire W, et al. Biochem Biophys Acta, 362:188-200, 1974.
105. Fung BM, Puon PS. Biophys J, 33:27-37, 1981.

Acknowledgements

It is of course a pleasure to acknowledge the efforts of those people without whom this thesis would not have been possible. Heading this list is Professor Alan Nelson of the Nuclear Engineering Department of M.I.T., my thesis supervisor. Alan has in many helpful ways directed my graduate career at M.I.T., and has given continuous support and encouragement for my work at M.G.H. His guidance was essential to the success of this project.

At the M.G.H., Dr. Ian Pykett was during his tenure there my mentor and primary source of NMR knowledge. It was his idea to begin the project of chemical shift imaging, and he carried out the earliest experiments. His expertise, especially during the development phase of this work, was without question crucial. More important, it was freely given in a true spirit of camaraderie and shared learning. The time I spent with Ian was some of the most rewarding in my academic career to date.

Also deserving special recognition is Dr. Thomas Brady, Director of Clinical NMR at the M.G.H. Tom has been a steadfast friend throughout my term at M.G.H. The faith and trust he has shown in my abilities and the opportunities he has attended me have allowed me to grow personally as well as professionally. Every graduate student should be so lucky as

to have a guardian angel as good humored and capable as Tom Brady.

Also at the M.G.H., Dr. David Chesler has acted as a constant resource and fund of knowledge. He has courageously tackled problems in fields he was ill acquainted with previously and has been patient both in acquiring the necessary facts and in presenting the answers. His door has always been open for questions, even when poorly formulated. His role in this work was truly special and beyond the call of duty.

At Harvard, Professor James Moran rounds out the list of my thesis committee. Although not directly involved with this work, he has taken on the role of "outsider" with his typical easy grace. He has for years been a good friend, and his willingness to help out and spirit of adventure were both well in character and much appreciated.

Of course, many others, both at M.I.T. and at M.G.H., contributed significantly to this work and my graduate career. Professor Ernie Cravalho of M.I.T., as director of the M.E.M.P. program there, was always supportive. It was he who introduced me to Alan Nelson, and so in many ways led to my work in NMR. Dr. Juan Taveras, Chairman of the Department of Radiology at M.G.H., has also been very supportive of my role as researcher/clinician. His generosity has helped me attend numerous scientific meetings, providing excellent

opportunities to meet other scientists doing NMR research. Dr. Jeffrey Newhouse, currently at the Columbia-Presbyterian Hospital in New York, single-handedly enlisted me into the NMR program at M.G.H. when others said it couldn't be done. He provided my first contact with NMR research, was always available for questions, and was a good friend. Drs. Ferdi Buonanno and Carl Kramer of Neurology provided important insight and expertise into the studies of the cat brain and neuromuscular disease. Dr. Ed Carter provided the animal model for the fatty liver studies, performed the biochemical analysis, and was in general helpful and good humored. Drs. Van Wedeen and Robert Oot assisted on a number of technical projects and deserve special recognition as friends and colleagues. Technical help was patiently provided by Paul Beaulieu and Karin Elmden; nothing in our laboratory could get accomplished without their hard work. Administrative assistance was graciously provided by Dee Dee Correia, Rita Zollo and Marlene Gillis. Finally, Edith Bell deserves special recognition for help in preparing this manuscript. She is a proficient typist, can spell, and can read my handwriting, all traits which set her apart from me and for which I am sincerely grateful. To all these people, thank you.